UNCLASSIFIED

AD 273 995

Reproduced
by the

ARMED SERVICES TECHNICAL INFORMATION AGENCY
ARLINGTON HALL STATION
ARLINGTON 12, VIRGINIA

UNCLASSIFIED

NOTICE: When government or other drawings, specifications or other data are used for any purpose other than in connection with a definitely related government procurement operation, the U. S. Government thereby incurs no responsibility, nor any obligation whatsoever; and the fact that the Government may have formulated, furnished, or in any way supplied the said drawings, specifications, or other data is not to be regarded by implication or otherwise as in any manner licensing the holder or any other person or corporation, or conveying any rights or permission to manufacture, use or sell any patented invention that may in any way be related thereto.

62-3-1

(10)

UNCLASSIFIED
AS AD NO. 273995

TECHNICAL REPORT #9

Contract NONR-2216 (11)

Project NR 017-630

Supervisor: Professor W. Kohn

University of California, San Diego

La Jolla, California

ASTIA
RECEIVED
APR 9 1962
TISIA

The United States Government is permitted the right to reproduce in whole or in part, for any purpose, the material herein contained.

IMAGES OF THE FERMI SURFACE IN PHONON AND SPIN-WAVE SPECTRA

E. J. Woll, Jr.

University of California, San Diego, La Jolla, California

TABLE OF CONTENTS

LIST OF FIGURES

Figure

ACKNOWLEDGEMENTS

The inspiration and support of Professor Walter Kohn are gratefully acknowledged. Dr. Stephen J. Nettel, who collaborated with the author on the spin-wave calculations, is likewise to be thanked. Valuable conversations have been held with Professors L. Onsager, J. Luttinger and H. Suhl, and with Drs. S. H. Vosko, J. S. Langer, N. R. Werthamer, J. des Cloizeaux, and A. Houghton. Drs. B. N. Brockhouse and S. Koenig are to be thanked for their communication of early experimental results; Professors V. Heine and H. Brooks have provided valuable opinions.

The author wishes especially to acknowledge the support of the National Science Foundation, and the hospitality of the University of California, at whose La Jolla campus much of this work was carried out.

ABSTRACT

Calculations are carried out to determine whether images of the electronic Fermi surface might be observable in phonon and spin-wave spectra of metals. Semi-quantitative estimates are made of the magnitude of image effects in phonon dispersion curves and phonon lifetimes in typical metals, as well as in spin-wave dispersion curves in rare-earth metals. These estimates lead to the conclusion that Fermi surface images may be experimentally observable in favorable circumstances.

INTRODUCTION

It is well known that the conduction electrons in a metal have an important influence on the effective force between the ion cores. Similarly, there now exists good evidence[1] that in some strongly magnetic metals the effective interaction between ionic spins is in large measure due to the mediation of the conduction electrons. It has been suggested that, as a result of these roles of the conduction electrons, phonon and spin-wave spectra should exhibit anomalies which reflect with geometric exactitude the shape of the Fermi surface.[2,3] These anomalies are referred to as images of the Fermi surface. They have been experimentally observed in the phonon spectrum of lead by Brockhouse et al.[4]

The influence of the conduction electrons on the effective force between two ion cores can be described in a simple way. Displacement of an ion from its equilibrium position virtually excites an electron-hole pair through coulomb interaction, and the pair then recombines by interaction with a second ion. Calculation of the energy due to this process, with ion positions considered as parameters, gives an effective potential energy of interaction between two ion cores. The influence of the conduction electrons on the interaction between ionic spins can be found similarly. An ion is able to excite a virtual electron-hole pair by coulomb exchange between a conduction electron and one of the ion's unpaired electrons. The electron-hole pair recombines by interaction with a second ion, and again the energy due to this process, with ionic spin orientations taken as parameters, gives an effective Hamiltonian

for interaction between ionic spins.

If the ions are displaced, or their spins are oriented, in such a way that a wave of wavenumber $\underline{q}$ propagates through the lattice, only electron-hole pairs of wavenumber $\underline{q}+\underline{K}$ will be created, where $\underline{K}$ is any vector of the reciprocal lattice. As the energies of phonon and spin-wave excitations are small compared to the electronic Fermi energy, the energy difference between the states of the whole system before and after virtual creation of an electron-hole pair is, to a good approximation, just the energy of the electron-hole pair. For small enough $\underline{q}+\underline{K}$, as is shown in Fig. 1 for a spherical Fermi surface, it is possible for electron-hole pairs of zero energy to be created, but for $\underline{q}+\underline{K}$ too large the lowest energy pair that can be created has finite energy proportional (in the case of a spherical Fermi surface) to $|\underline{q}+\underline{K}|$ ($|\underline{q}+\underline{K}|-2k_F$).

As $\underline{q}$ varies, then, zero energy pair creation abruptly becomes impossible on surfaces S in $\underline{q}$-space, determined by

1) $\underline{q} + \underline{K} = 2\underline{k}_o$

where $\underline{q}$ is a wave vector on S and $\underline{k}_o$ is on the Fermi surface. The strength of the effective interaction mediated by the electrons therefore sharply decreases, and the interaction between ions changes suddenly, on the surfaces S. For phonons, for instance, when the vector $\frac{1}{2}(\underline{q}+\underline{K})$ passes with increasing $\underline{q}$ from inside to outside the Fermi surface, electron shielding of the ions will be sharply reduced, so forces between the ions will become stronger. Then the phonon frequency will sharply increase on the surfaces S in $\underline{q}$-space. On the other hand, if $\frac{1}{2}(\underline{q}+\underline{K})$ passes from outside to inside the Fermi surface with increasing $\underline{q}$,

frequency will sharply decrease. Similar anomalies will occur in spin wave frequencies.

Because real pair creation cannot occur without conservation of energy, it is apparent that the lattice abruptly loses the ability to give energy to the electron gas whenever $\underline{q}$ passes through one of the surfaces S. Thus the lifetimes of phonons or spin-waves, considered as functions of $\underline{q}$, should show sharp breaks on the surfaces S.

In Part I we calculate, using simple models, dispersion curves and lifetimes for phonons in a typical metal, and in Part II we calculate dispersion curves for spin waves in the rare earth metals. The dispersion curve anomalies are shown to be logarithmic infinities in the derivative of frequency with $\underline{q}$, and the decay rates are shown to display step-discontinuities. The magnitudes of these effects are estimated.

These anomalies may in favorable circumstances be observed by neutron or X-ray diffraction measurements. Their observation should prove very valuable, as the location of the anomalies gives, by the simple construction of Eq. (1), quite direct information of the shape of the Fermi surface.

I. IMAGES OF THE FERMI SURFACE IN PHONON DISPERSION CURVES AND PHONON LIFETIMES IN METALS

Fermi surface images in phonon dispersion curves for lead have been experimentally observed, as mentioned in the Introduction, by Brockhouse et al.[4] This group has alsc reported that no image effects could be detected in the spectrum of sodium.

Here we attempt to make semi-quantitative estimates of the size of image effects in phonon spectra. In Sec. A phonon dispersion curves are calculated for a metal pictured as an array of ions immersed in and screened by a uniform gas of conduction electrons. The magnitude of the calculated image effects is comparable to that observed in lead.[4]

Sec. B refines this model to take into account the Bloch character of the electron wave functions. Using assumptions which are believed to be valid for certain metals, including sodium and aluminum, we find that this refinement reduces the image effects by a large factor, of order 10^{-2}. It may be remarked here that the magnitude of image effects is directly related to the magnitude of certain electron-phonon Umklapp processes.

In Sec. C we calculate the finite phonon lifetime resulting from decay by pair excitation. As a function of $\underline{q}$ this quantity displays step discontinuities which lie on the same surfaces S in $\underline{q}$ space as the frequency anomalies. These discontinuities may be experimentally observable in the widths of phonon frequencies.

A. The Uniform Electron Gas Model

The initial step in our calculation of dispersion curves is the determination of an effective potential of interaction between a pair of ions.

We first consider, following the calculation of Bardeen,[5] the electronic charge density built up when a single ion is placed in a uniform electron gas. Let the ion be situated at the coordinate origin, and denote the unscreened ionic potential by $QV(\underline{r})$, where Q is the

ionic charge. Then the Hartree Hamiltonian for an individual electron is

$$\text{I,1)} \quad H = H_o + Q_e V(\underline{r}) + e^2 V_e(\underline{r})$$

where H_o is the kinetic energy of the electrons, and $e^2 V_e(\underline{r})$ is the Hartree potential of interaction with the displaced electronic charge.* This potential must satisfy Poisson's equation

$$\text{I,2)} \quad \nabla^2 V_e(\underline{r}) = - 4\pi \, (N(\underline{r}) - N_o)$$

where $N(\underline{r})$ and N_o are, respectively, the perturbed and unperturbed electron densities. We introduce the volume of the crystal, Ω, and Fourier transforms according to the notation

$$\text{I,3)} \quad v(\underline{p}) = \int_{\Omega} V(\underline{r}) \, e^{-i\underline{p}\cdot\underline{r}} d^3r.$$

Then, by first order perturbation theory, the electron wavefunctions can be written as

$$\text{I,4)} \quad \Psi_{\underline{k}} = \Omega^{-\frac{1}{2}} \left(e^{i\underline{k}\cdot\underline{r}} + \Omega^{-1} \Sigma_{\underline{p}} \frac{Q_e v(\underline{p}) + e^2 v_e(\underline{p})}{E_{\underline{k}} - E_{\underline{k}+\underline{p}}} \; e^{i(\underline{k}+\underline{p})\cdot\underline{r}} \right)$$

where the $E_{\underline{k}}$ are unperturbed energies. From this expression $n(\underline{p})$ can be calculated. Substitution into the Fourier transform of Eq. (I,2) gives

$$\text{I,5)} \quad v_e(\underline{p}) = \frac{8\pi Q_e v(\underline{p}) \; W(\underline{p})}{p^2 + 8\pi e^2 W(\underline{p})}$$

where

$$\text{I,6)} \quad W(\underline{p}) = - \Omega^{-1} \Sigma_{k<k_F} \frac{1}{E_{\underline{k}} - E_{\underline{k}+\underline{p}}}$$

and the summation runs over the interior of the Fermi sphere of radius k_F.

---

*Because of the charge neutrality of the entire system, the zero wave number Fourier components of all potentials are consistently dropped.

This expression for $v_e(\underline{p})$ can be substituted into Eq. (I,4), and the electronic charge density $n(\underline{p})$ computed. The result is

$$\text{I,7)} \quad n(\underline{p}) = \frac{2Qep^2v(\underline{p})\ W(\underline{p})}{p^2 + 8\pi e^2 W(\underline{p})}$$

This is exactly the result found by Langer and Vosko.[6]

The interaction between two ions can now be viewed as having two parts: a direct interaction between the two ions, and an interaction of the second ion with the electronic charge density displaced by the first. The total interaction energy when the second ion is at $\underline{r}$ is then

$$\text{I,8)} \quad \Phi(\underline{r}) = \Omega^{-1}\Sigma_{\underline{p}}\varphi(\underline{p})\ e^{i\underline{p}\cdot\underline{r}}$$

where

$$\text{I,9)} \quad \varphi(\underline{p}) = (Q^2p^2v^2(\underline{p})/4\pi)\left(1 - \frac{8\pi e^2 W(\underline{p})}{p^2 + 8\pi e^2 W(\underline{p})}\right)$$

The first term describes direct interaction between the ions, and the second the reduction due to electronic screening.

Calculation of the vibration frequencies of a Bravais lattice is now simple. We denote the equilibrium position of the m'th ion by $\underline{R}_m$, and its excursion by $\underline{r}_m$. Then, to first order in the excursions, the force on the m'th ion is

$$\text{I,10)} \quad \underline{F}_m = -\Sigma_n \nabla_m \Phi_{mn} =$$
$$= -\Omega^{-1}\Sigma_{\underline{p}}\Sigma_n' e^{i\underline{p}\cdot(\underline{R}_m-\underline{R}_n)}\underline{p}\cdot(\underline{r}_m-\underline{r}_n)\ \underline{p}\varphi(\underline{p})$$

where Σ_n' goes over the N ions of the lattice, excluding m=n. The equations

of motion for the ions are

I,11) $\underline{F}_m = M \ddot{\underline{r}}_m$

where M is the ionic mass. Eqs. (I,10) and (I,11) are solved by the Ansatz

I,12) $\underline{r}_m = \underline{e} \cos(\underline{q}\cdot\underline{R}_m - \omega t)$

where $\underline{e}$ is a unit polarization vector, $\underline{q}$ the propagation vector, and

I,13) $\omega^2 = (N/M\,\Omega)\left[A(\underline{q}) + \Sigma_{\underline{K}\neq 0}\left(A(\underline{K}+\underline{q}) - A(\underline{K})\right)\right]$

The sum runs over all vectors of the reciprocal lattice, and

I,14) $A(\underline{p}) = (\underline{p}\cdot\underline{e})^2\,\varphi(\underline{p}) =$

$$= (Q^2/4\pi)\,(\underline{p}\cdot\underline{e})^2\,p^2v^2(\underline{p})\left(1 - \frac{8\pi e^2 W(\underline{p})}{p^2 + 8\pi e^2 W(\underline{p})}\right)$$

The Fermi surface images in the phonon dispersion curves arise from the character of the function $W(\underline{p})$. A straightforward integration of Eq. (I,6) yields for $W(\underline{p})$

I,15) $W(\underline{p}) = (m^* k_F/8\pi^2\hbar^2)\left(1 + \frac{4k_F^2 - p^2}{4k_F p}\ln\left|\frac{p+2k_F}{p-2k_F}\right|\right)$

A plot of $W(\underline{p})$ is presented in Fig. 2. It should be noted that the gradient of $W(\underline{p})$ has a logarithmic infinity at $p=2k_F$. The phonon frequency as defined by Eqs. (I,13) and (I,14) then has logarithmically infinite gradient with respect to $\underline{q}$ on the surfaces S in $\underline{q}$ space defined by

I,16) $|\underline{K}+\underline{q}| = 2k_F$

where $\underline{K}$ is any vector of the reciprocal lattice. Consequently, "kinks" occur in the dispersion curves on these surfaces. (In the more general

case of a non-spherical Fermi surface, Eq. (I,16) should be replaced by Eq. (1) of the introduction. The case of a non-spherical Fermi surface is treated somewhat more fully in Appendix 1.)

The dispersion curves (I,13) have been computed[7] for constants corresponding to aluminum, for propagation vectors in directions of high symmetry. Dispersion curves for $\underline{q}$ in the (111) direction of reciprocal space, for both directions of polarization, are plotted in Fig. 3. While the model of this section almost certainly overestimates the prominence of image effects in aluminum, (see Sec. B) the qualitative similarity of Fig. 3 to the observed phonon spectrum in lead (Fig. 4) is quite striking.

B. Bloch Electrons in the Bardeen Approximation

In a classic paper on electrical conductivity of metals, Bardeen[5] succeeded in treating the interaction of lattice vibrations with Bloch electrons by making certain simplifying assumptions about the electron wavefunctions. In this section we estimate the magnitude of image effects under the same assumptions.

We first calculate the change in electronic charge density set up when one ion of the lattice is displaced from its equilibrium position. We take as electron Hamiltonian

$$\text{I,17)} \quad H = H_o + Qe\, \underline{r}_1 \cdot \nabla V(\underline{r}) + e^2 V_e(\underline{r})$$

where H_o contains the electron kinetic energy, the energy of interaction with the ions in their equilibrium positions, and the Hartree interaction with the other Bloch electrons; $\underline{r}_1$ is the displacement of ion 1 from its

equilibrium position at the origin; $Q_e V(\underline{r})$ is the ionic potential and $e^2 V_e(\underline{r})$ is the self-consistent electron potential due to displacement of the ion.

We first assume, following Bardeen,[5] that the matrix element $(\underline{k}+\underline{p}|\nabla V(\underline{r})|\underline{k})$, taken between Bloch states, has negligible $\underline{k}$ dependence. (This is certainly so if the Bloch functions can be written in the form $u_o(\underline{r})\, e^{i\underline{k}\cdot\underline{r}}$.) We then define $v^*(\underline{p})$ according to the equation

I,18) $$\underline{p}\, v^*(\underline{p}) \equiv -i\,\Omega\,(\underline{k}+\underline{p}|\nabla V(\underline{r})|\underline{k})$$

At this point, to avoid making a fully self-consistent calculation with the Bloch functions, we recognize that the important effect of the term $e^2 V_e(\underline{r})$ is the screening of the ionic potential, and we follow Bardeen[5] in saying that screening by Bloch electrons will be roughly the same as free-electron screening. Then, instead of keeping the term $e^2 V_e(\underline{r})$ in Eq. (I,17), we simply reduce $v^*(\underline{p})$ by the factor $p^2/(p^2+8\pi e^2 W(\underline{p}))$. Since the effect of the screening is large only for small $\underline{p}$ while our region of interest is $p \sim 2k_F$, we do not expect this approximation to affect our results seriously.

With these assumptions the electron wavefunctions, perturbed by the displacement of ion 1, become

I,19) $$\Psi_{\underline{k}} = \varphi_{\underline{k}} + 4\pi Q_e\, \Omega^{-1} \Sigma_{\underline{p}} \frac{1}{E_{\underline{k}} - E_{\underline{k}+\underline{p}}}\, \underline{r}_1 \cdot i\underline{p}\, v^*(\underline{p})\, \frac{p^2}{p^2 + 8\pi e^2 W(\underline{p})}\, \varphi_{\underline{k}+\underline{p}}$$

where $\varphi_{\underline{k}}$ are the Bloch functions and $E_{\underline{k}}$ are the eigenvalues of H_o.

A second displaced ion interacts electrostatically with the first ion and the displaced electron charge. The energy of interaction with

the second ion at $\underline{R}_2+\underline{r}_2$ is

$$\text{I,20)}\quad \Phi_{12}=\frac{Q^2}{4\pi\Omega}\sum_{\underline{p}} e^{i\underline{p}\cdot(\underline{R}_1-\underline{R}_2)}\left(e^{i\underline{p}\cdot(\underline{r}_1-\underline{r}_2)}\ p^2v^2(\underline{p})-(\underline{p}\cdot\underline{r}_1)(\underline{p}\cdot\underline{r}_2)\frac{8\pi e^2W(\underline{p})p^2v^{*2}(\underline{p})}{p^2+8\pi e^2W(\underline{p})}\right)$$

where again the first term describes direct interaction between the ions, and the second term the reduction due to electron screening.

The calculation of vibration frequencies proceeds essentially as in Sec. A, and we find

$$\text{I,21)}\quad \omega^2=(N/M\,\Omega)\left[A(\underline{q})+\sum_{\underline{K}\neq 0}\left(A(\underline{K}+\underline{q})-A(\underline{K})\right)\right]$$

where

$$\text{I,22)}\quad A(\underline{p})=\frac{Q^2}{4\pi}(\underline{p}\cdot\underline{e})^2\left[p^2v^2(\underline{p})-\frac{8\pi e^2W(\underline{p})\ p^2v^{*2}(\underline{p})}{p^2+8\pi e^2W(\underline{p})}(1-\delta_{\underline{p},\underline{K}})\right]$$

Except for substitution of the factor $v^{*2}(\underline{p})(1-\delta_{\underline{p},\underline{K}})$ for $v^2(\underline{p})$, this result is identical to the result for the uniform electron gas model. The size of image effects is determined by the magnitude of $v^*(\underline{p})$ for $p=2k_F$. For sodium, Bardeen gives[5]

$$\text{I,23)}\quad Qev^*(\underline{p})=(C+4\pi Qe/p^2)\,G(pr_s)$$

where r_s is the radius of the unit cell approximated as a sphere, and

$$\text{I,24)}\quad G(x)=3x^{-3}(\sin x-x\cos x)\qquad G(0)=1$$

The constant C is related to the curvature of the Bloch functions near the edge of the unit cell, and is small (less than ten percent of $4\pi e^2/p^2$ in sodium for $p=2k_F$.)[8] Here we ignore C and note that the important modification of the result of the last section is a reduction of electron shielding terms by the factor $G^2(pr_s)$. Now $G^2(x)$ is a rapidly decreasing

function of x. In fact, for all metals $G(|\underline{K}+\underline{q}|r_s)$, with $\underline{q}$ in the first Brillouin zone and $\underline{K}\neq 0$, is small compared with unity, in general of order 10^{-1}. As a result, the electronic contribution to $A(\underline{p})$ (the second term in Eq. (I,22)) can be to a good approximation neglected in the $\Sigma_{\underline{K}}$ occurring in Eq. (I,21). In particular, the magnitude of the image effects is reduced by a factor of order 10^{-2}.

These considerations are in the same spirit as the discussion of the elastic constants of sodium by Bardeen and Pines,[8] who obtain agreement with experiment to within ten percent. Their results can be obtained from Eqs. (I,21) and (I,22) if the second term in (I,22) is dropped for $\underline{p}\neq\underline{q}$.

We expect this estimate of Bloch wave effects to be somewhat drastic. It is probably realistic for sodium and for certain other metals (including aluminum) whose characteristics are more fully discussed in Appendix 2. It should be noted that image effects are small in these cases for the reason that Umklapp processes do not make an important contribution to the electron-ion interaction. This should not be true in general. If, for some metals, Umklapp processes do make an important contribution, we should expect this fact to be reflected in some characteristics of the metal. Thus, clues may appear, from an examination of metallic characteristics, as to whether Fermi surface images are observable. Two such clues suggest themselves. First, resistivity of a metal with important Umklapp processes should be somewhat higher than is to be expected from simple scaling. Second, since only Umklapp processes screen the transverse lattice vibrations, metals in which Umklapp

processes are negligible will have transverse frequencies entirely determined by direct ionic interaction. We have, of course, neglected ion-overlap contributions to the frequency; so that transverse frequencies will be higher, by some unknown amount, than our formulas would predict; but at least the existence of unusually low transverse frequencies would imply that Umklapp processes were contributing.[9] In both of these characteristics, lead shows the properties of a metal with substantial Umklapp effects: the resistance is unusually high and the transverse frequencies, as judged by the Debye temperature, are unusually low. On the other hand, aluminum and sodium have resistance and Debye temperature in line with the usual run of metals.

In summary, the non-observation of image effects in sodium and aluminum is consistent with other empirical properties of these metals, and can also be concluded from a priori calculations. On the other hand, the observation of such effects in lead, while consistent with other empirical information, has not yet been explained on the basis of a detailed calculation.

C. Phonon Lifetime

Several decay mechanisms can contribute to shortening of the phonon lifetime, including interactions with other phonons and various processes which transfer energy to the electron gas. We here discuss the decay process which gives simple information about the shape of the Fermi surface; that is, decay of a phonon into a single electron-hole pair. In Appendix 3 decay rates for important competing decay processes are

estimated, and it is found that the single pair creation discussed here gives the most important contribution to phonon decay.

We find the lifetime of a phonon exposed to the hazard of decay into an electron hole pair by calculating the rate of energy absorption by the electron gas when the lattice is driven in one of its normal modes. We assume that the electrons see screened ions, so the electron-ion matrix element is taken to be reduced, as in Sec. B, by the factor $p^2/(p^2+8\pi e^2 W(\underline{p}))$. From first order perturbation theory, we find for the probability per unit time that the state $|\underline{k}+\underline{p})$ be excited from the state $|\underline{k})$, by interaction with an array of ions vibrating as in (I,12)

$$\text{I,25)}\quad W_{\underline{k}+\underline{p},\underline{k}} = (\pi N^2 Q^2 e^2/2\Omega^2\hbar^2)\,\frac{(\underline{p}\cdot\underline{e})^2\, p^4 v^{*2}(\underline{p})}{p^2 + 8\pi e^2 W(\underline{p})}\quad \delta_{\underline{p},\underline{K}+\underline{q}}\quad \times$$

$$\times\left(\delta(E_{\underline{k}+\underline{p}} - E_{\underline{k}} - \hbar\omega) + \delta(E_{\underline{k}+\underline{p}} - E_{\underline{k}} + \hbar\omega)\right)$$

The total energy absorbed per unit time by the electron gas is

$$\text{I,26)}\quad E' = \Sigma_{k<k_F}\,\Sigma_{\underline{p}}\;\; W_{\underline{k}+\underline{p},\underline{k}}\,(E_{\underline{k}+\underline{p}} - E_{\underline{k}})$$

where $\Sigma_{k<k_F}$ runs over all states below the Fermi surface, and $\Sigma_{\underline{p}}$ runs over all electron states. $W_{\underline{k}+\underline{p},\underline{k}}$ is, except for the energy δ-functions, independent of $\underline{k}$. Converting $\Sigma_{k<k_F}$ into an integration and doing the integration over the δ-functions gives a factor

$$\text{I,27)}\quad \begin{cases} m^{*2}\omega^2/2\pi^2\hbar^2 p & \text{for } p<2k_F \\ 0 & \text{for } p>2k_F \end{cases}$$

The total energy absorption per unit time, expressed as a fraction of the total vibrational energy of the lattice, can be identified as the

phonon decay rate, or inverse lifetime*

$$\text{I,28)}\quad 1/\tau = (Q^2 e^2 m^{*2} N/\pi\hbar^3 M\Omega) \sum_{\underline{K}} B(\underline{K}+\underline{q})$$

where

$$\text{I,29)}\quad B(\underline{p}) = \begin{cases} (\underline{p}\cdot\underline{e})^2\, p^3 v^{*2}(\underline{p}) / \left(p^2 + 8\pi e^2 W(\underline{p})\right) & \text{for } p<2k_F \\ 0 & \text{for } p>2k_F \end{cases}$$

The decay rates computed from Eqs. (I,28) and (I,29) display step-discontinuities on surfaces in $\underline{q}$ space defined by $|\underline{q}+\underline{K}| = 2k_F$. These decay rates have been computed, taking for $v^*(\underline{p})$ the nearly-free-electron matrix element, for constants corresponding to aluminum. Curves for both directions of polarization for $\underline{q}$ in the (111) direction of reciprocal space are plotted in Fig. 5.

Again it should be noted that, if $v^*(\underline{p})$ falls off faster than the nearly-free-electron approximation predicts, the magnitude of the discontinuities will be correspondingly reduced. In particular, for the case of sodium and aluminum, only the $\underline{K}=0$ term should appreciably contribute in Eq. (I,28), and no significant breaks should appear.

II. IMAGES OF THE FERMI SURFACE IN SPIN-WAVE DISPERSION CURVES AND SPIN-WAVE LIFETIMES IN RARE EARTH METALS

The rare earth metals from gadolinium to thulium are expected to be good subjects for detection of Fermi surface images in spin-wave

---

*Neglecting Umklapp processes, this result agrees with Pippard's[10] result for attenuation of ultrasonic waves, in the limit where $\underline{q}$ is small, though not so small as the reciprocal electron mean free path from impurity scattering.

dispersion curves. This expectation arises because, in view of the smallness of the 4f shell in these metals, overlap between 4f shells of neighboring ions should be quite small. The ionic spins can then be expected to be coupled primarily through exchange scattering of conduction electrons.[11,12,13]

In this section we develop an effective Hamiltonian for interaction between ionic spins, first choosing suitable ionic potentials for interaction between conduction electrons and ionic spins. The change in total energy of the system due to these interactions is then found by a perturbation calculation carried out to second order, paralleling the calculation of de Gennes[12] for Curie temperatures of the rare earths and the calculation of Ruderman and Kittel[11] for the coupling of nuclear spins. The effective Hamiltonian for interaction of ionic spins takes the form of a sum of Heisenberg scalar product interactions. The spin-wave excitations are found by usual methods.[14]

Approximate numerical calculations of the spin-wave frequencies as functions of wave vector $\underline{q}$ are carried out for directions of high symmetry, so that magnitudes of the anomalies can be estimated. Throughout the discussion it is assumed that the ground state of the ion spin system is ferromagnetic. The extension of our results to the antiferromagnetic case is taken up, briefly, in Appendix 4.

Because of the small radius of the 4f shell, we take the exchange interaction between conduction electrons and ionic spin to have δ-function spatial dependence. The single electron Hamiltonian can then be written

II,1) $H = G\Sigma_m \delta(\underline{R}_m - \underline{r})\, \underline{J}_m \cdot \underline{S}$

where $\underline{J}_m$ and $\underline{S}$ are, respectively, the angular momentum operator for the m'th ion and the electron spin operator. $\underline{R}_m - \underline{r}$ is the displacement of the electron relative to the position $\underline{R}_m$ of the m'th ion; the sum runs over all N ions of the lattice. The scalar product form $\underline{J}_m \cdot \underline{S}$ has been discussed by Kasuya[13] and by Liu.[15] The interaction (II,1) has been postulated by de Gennes and Friedel[1] in their calculation of spin-disorder resistivity in gadolinium; they were able to deduce an approximate value for the coupling constant G from experimental resistivities. De Gennes[12] has suggested that, for the metals from gadolinium to thulium, G can be taken proportional to (g-1)J, where g is the Landé factor.

The effective Hamiltonian for the ionic spins is found by calculating the energy of the electron gas in a given configuration of ionic spins. The part of this energy which couples the spins of different ions is, to lowest order in the coupling constant G,

II,2) $$H_{eff} = -G^2 \Sigma_{k<k_F, s} \Sigma_{\underline{p}, s'} \frac{1}{E_{\underline{k}+\underline{p}} - E_{\underline{k}}} \times$$

$$\times \left(\underline{k}, s \middle| \Sigma_m \delta(\underline{R}_m - \underline{r})\, \underline{J}_m \cdot \underline{S} \middle| \underline{k}+\underline{p}, s'\right) \left(\underline{k}+\underline{p}, s' \middle| \Sigma_n \delta(\underline{R}_n - \underline{r})\, \underline{J}_n \cdot \underline{S} \middle| \underline{k}, s\right)$$

where $\Sigma_{k<k_F, s}$ runs over all electron states, characterized by momentum $\hbar\underline{k}$ and z-component of spin s, which lie beneath the Fermi surface, and $\Sigma_{\underline{p}, s'}$ runs over all electron states. Σ'_n runs over the N ions of the lattice, excluding m=n. The energies $E_{\underline{k}}$ have been taken to be spin independent. Performing the spin sums and evaluating the matrix elements gives

II,3) $H_{eff} = -\frac{1}{2} G \Sigma_m \Sigma'_n \underline{J}_m \cdot \underline{J}_n F(\underline{R}_m - \underline{R}_n)$

$F(\underline{R}_m-\underline{R}_n)$ is the long range oscillating interaction introduced by Ruderman and Kittel,[11] and is given by

II,4) $$F(\underline{r}) \equiv \Omega^{-2}\Sigma_{\underline{p}}\, e^{i\underline{p}\cdot\underline{r}}\, \Sigma_{k<k_F} \frac{1}{E_{\underline{k}+\underline{p}}-E_{\underline{k}}}$$

where Ω is the volume of the crystal.

We now substitute into Eq. (II,3) the Holstein-Primakoff operators a_m^*, a_m, defined by[14]

II,5) $$(2J)^{\frac{1}{2}}(1 - a_m^*a_m/2J)^{\frac{1}{2}}\, a_m = J_{mx} + iJ_{my}$$

$$(2J)^{\frac{1}{2}}a_m^*(1 - a_m^*a_m/2J)^{\frac{1}{2}} = J_{mx} - iJ_{my}$$

$$J - a_m^*a_m = J_{mz}$$

The resulting expression can be expanded to give terms of 0'th, 2nd, 4th, ... order in the field operators. We omit terms of higher than second order. (The higher order terms represent interactions between spin waves, and give no contribution when only one spin wave is present in the lattice.) Then

II,6) $$H_{eff} = -\tfrac{1}{2}G^2J^2\Sigma_m\, \Sigma_n'\; F(\underline{R}_m-\underline{R}_n)\left[1 + (2/J)(-a_m^*a_m + a_m^*a_n)\right]$$

The hexagonal-close-packed structure of the rare earths requires that a distinction be made between the two types of lattice site. We regard the ions as lying on two hexagonal Bravais lattices, whose relative displacement is given by the vector $\underline{D}$. The position of an ion on the first lattice will continue to be written as $\underline{R}_m$, m= 1, 2, ..., $\frac{1}{2}$N; and the corresponding spin operators will be written as $a_m^{*(e)}$, $a_m^{(e)}$. For the second lattice the position and spin operators will be $\underline{R}_m+\underline{D}$ and $a_m^{*(o)}$, $a_m^{(o)}$. We substitute into Eq. (II,6) the transformations

II,7) $$a_m^{(e)} = (2/N)^{\frac{1}{2}} \Sigma_{\underline{q}} e^{i\underline{q}\cdot\underline{R}_m} a_{\underline{q}}^{(e)}$$
$$a_m^{(o)} = (2/N)^{\frac{1}{2}} \Sigma_{\underline{q}} e^{i\underline{q}\cdot(\underline{R}_m+\underline{D})} a_{\underline{q}}^{(o)}$$

Here the sums run over all wave vectors $\underline{q}$ in the first Brillouin zone of the hexagonal Bravais lattice. Omitting the constant term in Eq. (II,6) we get

II,8) $$H_{eff} = G^2 J \Sigma_{\underline{q}} \left[A_{\underline{q}} \left(a_{\underline{q}}^{*(e)} a_{\underline{q}}^{(e)} + a_{\underline{q}}^{*(o)} a_{\underline{q}}^{(o)} \right) - B_{\underline{q}} a_{\underline{q}}^{*(e)} a_{\underline{q}}^{(o)} - B_{\underline{q}}^{*} a_{\underline{q}}^{*(o)} a_{\underline{q}}^{(e)} \right]$$

where

II,9) $$A_{\underline{q}} = \Sigma_{\underline{R}} \left(F(\underline{R}) + F(\underline{R}+\underline{D}) - F(\underline{R})\, e^{i\underline{q}\cdot\underline{R}} \right)$$
$$B_{\underline{q}} = \Sigma_{\underline{R}}\, F(\underline{R}+\underline{D})\, e^{i\underline{q}\cdot(\underline{R}+\underline{D})}$$

Here the sums run over all the displacements $\underline{R}$ of a single Bravais lattice, including $\underline{R}=0$.

Finally, to diagonalize the Hamiltonian given by Eq. (II,8), we use

II,10) $$b_{\underline{q}} = 2^{-\frac{1}{2}} \left[a_{\underline{q}}^{(e)} + (B_{\underline{q}}/|B_{\underline{q}}|)\, a_{\underline{q}}^{(o)} \right]$$
$$c_{\underline{q}} = 2^{-\frac{1}{2}} \left[a_{\underline{q}}^{(e)} - (B_{\underline{q}}/|B_{\underline{q}}|)\, a_{\underline{q}}^{(o)} \right]$$

The result is

II,11) $$H_{eff} = G^2 J \Sigma_{\underline{q}} \left[b_{\underline{q}}^{*} b_{\underline{q}} (A_{\underline{q}} - |B_{\underline{q}}|) + c_{\underline{q}}^{*} c_{\underline{q}} (A_{\underline{q}} + |B_{\underline{q}}|) \right]$$

For simplicity, our computations will be limited to the "acoustical" spin waves, whose frequencies are given by

II,12) $$\hbar\omega = G^2 J\, (A_{\underline{q}} - |B_{\underline{q}}|).$$

To carry out the computations, we need the Fourier transform of $F(\underline{R})$, which, by inspection of the definition (II,4) of $F(\underline{R})$, is just

II,13) $$\Omega^{-1} \Sigma_{k<k_F} \frac{1}{E_{\underline{k}+\underline{p}} - E_{\underline{k}}} = W(\underline{p})$$

where $W(\underline{p})$ is just the function encountered in the treatment of phonon dispersion curves, (plotted in Fig. 2) which has logarithmically infinite gradient at $p=2k_F$. When the lattice sums indicated in Eq. (II,9) are carried out, we find

$$\text{II,14)} \quad A_{\underline{q}} = \tfrac{1}{2}(N/\Omega)\,\Sigma_{\underline{K}} \left(W(\underline{K}+\underline{q}) - W(\underline{K}) - W(\underline{K})\cos(\underline{K}\cdot\underline{D})\right)$$

$$B_{\underline{q}} = \tfrac{1}{2}(N/\Omega)\,\Sigma_{\underline{K}}\; W(\underline{K}+\underline{q})\; e^{i\underline{K}\cdot\underline{D}}$$

with the sums running over all vectors $\underline{K}$ of the reciprocal lattice.

The spin wave frequencies are obtained by substituting Eq. (II,14) into Eq. (II,12). The reciprocal vectors form a hexagonal lattice. For wave vectors pointing in the direction of the c-axis in reciprocal space, the formula for the acoustical frequencies takes the particularly simple form

$$\text{II,15)} \quad \hbar\omega = G^2 J(N/2\Omega)\Sigma_{\underline{K}} \left(W(\underline{K}+\underline{q}) - W(\underline{K})\right)\left(1 - \cos(\underline{K}\cdot\underline{D})\right)$$

Approximate numerical computations of the dispersion curve in the directions of the c and a axes have been carried out. The results are shown in Fig. 6. Discrete sums over the first 307 points in reciprocal space were taken. The sum $\Sigma_{\underline{K}} \left(W(\underline{K}+\underline{q}) - W(\underline{K})\right)\; e^{i\underline{K}\cdot\underline{D}}$ was found to converge sufficiently rapidly that more distant points could be neglected. The sum $\Sigma_{\underline{K}} \left(W(\underline{K}+\underline{q}) - W(\underline{K})\right)$ over the more distant points was approximated by a suitable integral.

As in the phonon case, the frequencies defined by Eqs. (II,12) and (II,14) have logarithmically infinite gradient with respect to $\underline{q}$ on the surfaces S in $\underline{q}$ space defined by Eq. (I,16) or Eq. (1) of the Introduction. Consequently, "kinks" occur in the dispersion curves on these surfaces.

From the computed curve, these kinks can be seen to be of the order of two percent of the maximum spin wave frequencies. They appear, therefore, to be within the range of experimental detection.

It will be observed that the frequencies become negative for $\underline{q}$ in the c direction. The calculations have the feature that the frequencies are extremely sensitive, both in magnitude and sign, to small changes in the shape of the Fermi surface. However, the magnitude of the kinks is not seriously affected by such changes. The implications of negative dispersion curves are discussed more fully in Appendix 4.

A few remarks about the effects of finite ion size seem in order. This effect is extremely difficult to treat quantitatively. However, it should be noticed that to some extent the effect is allowed for in the determination of G from observed resistivities, and that the dimensionless parameter that measures the importance of the effect, namely $k_F r_o$, where r_o is the "radius" of the 4f shell, has the approximate value 0.4. It is, therefore, not to be expected that our estimate of the relative size of Fermi surface images is seriously in error.

It should be noted that the appearance of Fermi surface images in the spin-wave dispersion curves is in no way dependent on the special features of the rare earth metals. In general, the conduction electrons of a metal can be expected to take some part in the interaction between ionic spins, so "kinks" should appear in the spin-wave dispersion curves. Their relative size will, however, be reduced as the electrons play a less important part in the total interaction between ionic spins.

Fermi surface image effects in the spin-wave lifetime will be mentioned only briefly here. The contribution to spin-wave decay rate of the process (spin-wave → electron-hole pair) can be evaluated straightforwardly, in direct analogy to the phonon case, and will give a decay rate which has step-discontinuities on the surfaces S in $\underline{q}$-space. Other contributions to the spin-wave decay rate are, however, not well understood,[16] so the relative size of the Fermi surface images is difficult to estimate.

APPENDIX 1

Connection Between Anomalies of Frequency and Decay Rate

We investigate in this appendix the relationship between phonon frequency and phonon decay rate, in order to clarify the connection between the two sorts of spectral anomaly. We shall find that a close relationship exists, connecting the nature and magnitude of Fermi surface images in the phonon dispersion curves with the nature and magnitude of Fermi surface images in the phonon decay rate curves.

In the dispersion curve calculations of Part I, it was assumed that ion motions were slow enough that screening electrons were able to follow a moving ion perfectly. In Sec. a of this appendix we relax this assumption, calculating the electron charge distribution time-dependently in a lattice of moving ions. The force exerted on a given ion by this electron charge distribution is found to be not altogether in phase with the position of the ion, so the ion does net work on the electron gas, and there is net transfer of energy into the electron gas from the vibrating lattice. The rate of energy absorption can be related to the phonon lifetime; the phonon decay rate curves and dispersion curves are then found to be given by real and imaginary parts of the same function.

In Sec. b the properties of the function which gives dispersion curves and decay rates are investigated for complex frequency ω. It is shown that "kinks" in the dispersion curve and breaks in the decay rate arise from the behavior of this function near a branch cut on the real

axis of the complex ω-plane. The relative magnitudes of the anomalies are compared.

In Sec. c the behavior of the phonon dispersion curves and phonon lifetimes is considered for the case of a non-spherical Fermi surface. It is shown that images of convex parts of the Fermi surface take the same forms as the images which occur in the case of a spherical Fermi surface. The relative magnitudes of frequency and decay rate anomalies are, however, found to be somewhat changed.

a. Calculation of Frequency and Decay Rate

We proceed to calculate the time-dependent electron charge distribution in a lattice where the ionic excursions are given by

A1) $\underline{r}_m = \underline{e} \cos(\underline{q}\cdot\underline{R}_m - \omega t)$

where $\underline{R}_m$ is the equilibrium position of the m'th ion. The electrons are assumed not to interact with each other, though the largest effect of electron-electron interaction is taken into account by assuming that the electrons see screened ions. An electron is thus assumed to see a potential $(eQ/r)\, e^{-ar}$ from an ion located at the origin. The constant a is taken to be the Thomas-Fermi screening parameter $(2k_F/\pi a_o)^{\frac{1}{2}}$, where a_o is the Bohr radius.[6]

The time dependent electron wave functions can be written

A2) $\Psi_{\underline{k}}(\underline{r},t) = \Omega^{-\frac{1}{2}} \left(e^{i[\underline{k}\cdot\underline{r} - E_{\underline{k}}t/\hbar]} + \Sigma_{\underline{p}}\, a_{\underline{k}+\underline{p},\underline{k}}(t)\, e^{i[(\underline{k}+\underline{p})\cdot\underline{r} - E_{\underline{k}+\underline{p}}t/\hbar]}\right)$

where, from perturbation theory

A3) $a_{\underline{k}+\underline{p},\underline{k}}(t) = -(i/\hbar) \int_{-\infty}^{t} e^{\eta t'} e^{i(E_{\underline{k}+\underline{p}} - E_{\underline{k}})t'/\hbar} \langle \underline{k}+\underline{p} | Q\Sigma_m V(\underline{r}-\underline{R}_m-\underline{r}_m) | \underline{k} \rangle dt'$

The screened ion potentials $V(\underline{r})$ have been taken to be turned on slowly over a long period of time by the factor $e^{\eta t'}$. η will be taken small, so that $\eta t \ll 1$ for all times t of interest. The matrix element gives

A4) $$\langle \underline{k}+\underline{p} | Qe\Sigma_m V(\underline{r}-\underline{R}_m-\underline{r}_m) | \underline{k} \rangle =$$

$$= (QeN/\Omega)\frac{4\pi}{p^2+a^2}\left[\delta_{\underline{p},\underline{K}} + \tfrac{1}{2}i(\underline{p}.\underline{e})\left(\delta_{\underline{p},\underline{K}+\underline{q}}\, e^{-i\omega t'} + \delta_{\underline{p},-\underline{K}-\underline{q}}\, e^{i\omega t'}\right)\right]$$

and after doing the time integrations the electron charge density can be found to be

A5) $$eN_e(\underline{r},t) = (QN/\Omega) + (QN/2\Omega)\,\Sigma_{\underline{p}}\ \frac{4\pi e^2}{p^2+a^2}\ e^{i\underline{p}\cdot\underline{r}}\ \times$$

$$\times\Bigg\{ i\underline{p}\cdot\underline{e}\left[\delta_{\underline{p},\underline{K}+\underline{q}}\left(W(\underline{p},\omega,\eta) + W(\underline{p},-\omega,-\eta)\right)\, e^{-i\omega t} + \right.$$

$$\left. + \delta_{\underline{p},-\underline{K}-\underline{q}}\left(W(\underline{p},-\omega,\eta) + W(\underline{p},\omega,-\eta)\right)\, e^{i\omega t}\right] +$$

$$- \delta_{\underline{p},\underline{K}}\left(W(\underline{p},0,\eta) + W(\underline{p},0,-\eta)\right)\Bigg\}$$

where

A6) $$W(\underline{p},\omega,\eta) \equiv \Omega^{-1}\,\Sigma_{k<k_F}\,\frac{1}{E_{\underline{k}+\underline{p}}-E_{\underline{k}}-\hbar(\omega+i\eta)}$$

We again view the potential energy of the ion at the origin as being made up of two parts: a direct interaction potential from all the other ions, and a potential energy of interaction with the displaced electron charge distribution. The potential energy of this ion is given by

A7) $$\Phi(\underline{r}_1) = \int_\Omega QV_I(\underline{r}-\underline{r}_1)\cdot\left(\Sigma_m\, QN(\underline{r}-\underline{r}_m-\underline{R}_m) + eN_e(\underline{r},t)\right)\ d^3r$$

where $QV_I(\underline{r})$ and $QN(\underline{r})$ are, respectively, the electrostatic potential and charge density of an ion situated at the origin. For point ions, we find for the force acting on the ion at the origin

$$\text{A8)}\quad \underline{F}_1 = -\nabla\Phi_1 = (4\pi Q^2 N/\Omega)\ \Sigma_{\underline{p}}\ \frac{1}{p^2}\ \underline{p}\ (\underline{p}\cdot\underline{e})\ \Bigg\{ (\delta_{\underline{p},\underline{K}} - \delta_{\underline{p},\underline{K}+\underline{q}})\ \cos\omega t\ +$$

$$\frac{4\pi e^2}{p^2+a^2}\ \Big[\ \delta_{\underline{p},\underline{K}}\ \Big(W(\underline{p},0,\eta) + W(\underline{p},0,-\eta)\Big)\ \cos\omega t\ +$$

$$-\ \delta_{\underline{p},\underline{K}+\underline{q}}\ \mathrm{Re}\ \{W(\underline{p},\omega,\eta) + W(\underline{p},-\omega,-\eta)\}\ \cos\omega t\ +$$

$$-\ \delta_{\underline{p},\underline{K}+\underline{q}}\ \mathrm{Im}\ \{W(\underline{p},\omega,\eta) + W(\underline{p},-\omega,-\eta)\}\ \sin\omega t\ \Big]\Bigg\}$$

The force is seen to be somewhat out of phase with $\underline{r}_1$. The $\sin\omega t$ term in $\underline{F}_1$ will cause energy dissipation, and implies that (A1) does not solve the equations of motion exactly for the lattice. But if the energy dissipation is slow enough, compared to ω, (A1) will still give a nearly exact solution. In this case, which is the case of interest, we can identify the $\cos\omega t$ term in $\underline{F}_1$ as the driving force on the ion, and the $\sin\omega t$ term as a dissipative force. Frequencies are then calculated as in Part I. The rate of energy dissipation per unit energy is

$$\text{A9)}\quad 1/\tau = (1/M\omega^2)(\omega/2\pi)\int_0^{2\pi/\omega} \underline{F}_1\cdot\dot{\underline{r}}_1\,dt =$$

$$= (4\pi Q^2 N/2M\omega\Omega)\ \Sigma_{\underline{p}}\ \frac{4\pi e^2}{p^2(p^2+a^2)}\ (\underline{p}\cdot\underline{e})^2\ \mathrm{Im}\{W(\underline{p},\omega,\eta)+W(\underline{p},-\omega,-\eta)\}$$

The expressions for frequency and decay rate can be combined into the expression

$$\text{A10)}\quad \omega^2 + 2i\omega/\tau = B(\underline{q},\underline{e},\omega)$$

where

$$\text{A11)}\quad B(\underline{q},\underline{e},\omega) = (4\pi Q^2 N/M\Omega)\ \Sigma_{\underline{p}}\ \frac{1}{p^2}\ (\underline{p}\cdot\underline{e})^2\ \times$$

$$\times\ \lim_{\eta\to 0}\Bigg\{\delta_{\underline{p},\underline{K}+\underline{q}}\Big[1 - \frac{4\pi e^2}{p^2+a^2}\ \Big(W(\underline{p},\omega,\eta)+W(\underline{p},-\omega,-\eta)\Big)\Big]\ +$$

$$-\ \delta_{\underline{p},\underline{K}}\Big[1 - \frac{4\pi e^2}{p^2+a^2}\ \Big(W(\underline{p},0,\eta)+W(\underline{p},0,-\eta)\Big)\Big]\Bigg\}$$

$1/\tau$ is to be identified as the phonon decay rate. The equations (A10) and (A11) determine ω implicitly, but we will find that, for frequencies of ordinary magnitude, the real part of $W(\underline{p},\omega,\eta)$ is to a very good approximation independent of ω.

We should note here that the derivation of Eq. (A10) has been more specialized than is necessary. In general, the time dependent electron density in the vibrating lattice can be written

$$A12)\quad N(\underline{r},t) = \Sigma_{\underline{K}} \Big(n_o(\underline{K})\, e^{i\underline{K}\cdot\underline{r}} + n_o^*(\underline{K})\, e^{-i\underline{K}\cdot\underline{r}} + n(\underline{K}+\underline{q},\omega) e^{i\,[(\underline{K}+\underline{q})\cdot\underline{r}-\omega t]} + n^*(\underline{K}+\underline{q},\omega) e^{-i\,[(\underline{K}+\underline{q})\cdot\underline{r}-\omega t]} \Big)$$

This form follows from the reality of $N(\underline{r},t)$ and from the fact that the electron gas can only take up crystal momentum $\underline{q}$ from the vibrating lattice. Using this form for the electron density, we arrive at a relation of the form of Eq. (A10).

b. Properties of the Function $W(\underline{p},\omega,\eta)$

In the example treated in Sec. a, the real and imaginary parts of the function $B(\underline{q},\underline{e},\omega)$ can be found by investigating the analytic structure of the function

$$A13)\quad W(\underline{p},\omega^+) = \lim_{\eta \to 0} W(\underline{p},\omega,\eta)$$

where the notation ω^+ means that ω is taken to have a vanishingly small positive imaginary part. $W(p,\omega^+)$ is defined by Eq. (A6) as a sum over energy denominators; converting the summation in (A6) into an integration gives

$$A14)\quad W(\underline{p},\omega^+) = (8\pi^3\hbar)^{-1} \int \left[(\hbar/m^*)(\underline{k}\cdot\underline{p} + \tfrac{1}{2}p^2) - \omega^+ \right]^{-1} d^3k$$

where the integration runs over all $\underline{k}$ such that $k<k_F$. This integral, considered as a function of complex ω (parametrized by $\underline{p}$), has a branch cut on the real axis of the complex ω-plane. The imaginary part of $W(\underline{p},\omega^+)$ is just

A15) $$\text{Im}\{W(\underline{p},\omega^+)\} = (8\pi^2\hbar)^{-1}\int \delta\left[(\hbar/m)(\underline{k}\cdot\underline{p} + \tfrac{1}{2}p^2) - \omega\right] d^3k$$

This integration can be performed simply, but in order to clarify the general features of the problem we picture the integration in Fig. A1. The dashed line in Fig. A1 represents the surface R in $\underline{k}$-space where, for fixed $\underline{p}$ and ω, the energy denominator in the integrand of Eq. (A14) vanishes. The integration for the imaginary part of $W(\underline{p},\omega^+)$ just runs over the area intersected by the Fermi surface on the surface R, and is proportional to this area. Now since the energy denominator is a linear function of $\underline{k}$ and ω, the position of the surface R travels linearly with ω as ω is varied. We call ω_o a value of ω for which R becomes tangent to the Fermi surface. Then as $\omega \to \omega_o$ in such a way that R goes from inside the Fermi surface to become tangent to it, the area intersected on R goes to zero linearly with $\omega - \omega_o$. Thus the imaginary part of $W(\underline{p},\omega^+)$ goes to zero linearly as $\omega \to \omega_o$. For values of ω for which R does not intersect the Fermi surface, $W(\underline{p},\omega^+)$ will have no imaginary part.

Performing the integration for $\text{Im}\{W(\underline{p},\omega^+)\}$ gives

A16) $$\text{Im}\{W(\underline{p},\omega^+)\} = \begin{cases} -(m^{*3}/8\pi\hbar^4p^3)\left[\omega - (\hbar/m^*)p(\tfrac{1}{2}p-k_F)\right]\left[\omega - (\hbar/m^*)p(\tfrac{1}{2}p+k_F)\right] \\ \qquad \text{... for } (\hbar/m^*)p(\tfrac{1}{2}p-k_F)<\omega<(\hbar/m^*)p(\tfrac{1}{2}p+k_F) \\ 0 \text{ for } \omega^+ \text{ outside this range.} \end{cases}$$

which, indeed, falls linearly to zero as ω approaches the values for which R is tangent to the Fermi surface.

The existence of an imaginary part of $W(\underline{p},\omega^+)$ just reflects the existence of the branch cut on the real axis of the ω-plane. From Eq. (A14) it follows that $W(\underline{p},\omega)$ has a discontinuity in its imaginary part as ω goes from above to below the branch cut; this discontinuity corresponds to a change in sign of the imaginary part. Then $\mathrm{Im}\{W(\underline{p},\omega^+)\}$ can be seen to have just half the value of this discontinuity.

From inspection of Eq. (A14) we see that $W(\underline{p},\omega)$ falls off as $1/\omega$ for large ω, and that the only non-analyticity in this function is the branch cut on the real axis. The real part of $W(\underline{p},\omega^+)$ can then be found by a simple contour integration. We can write

$$\text{A17)} \qquad \int_C \frac{W(\underline{p},s)}{s-\omega^+}\,ds = 0 = \int_{-\infty}^{+\infty} \frac{W(\underline{p},s^+)}{s-\omega^+}\,ds - i\pi W(\underline{p},\omega^+)$$

where C is the contour drawn in Fig. A2. Taking the imaginary part of Eq. (A17) gives

$$\text{A18)} \qquad \mathrm{Re}\{W(\underline{p},\omega^+)\} = (1/\pi) \int_{-\infty}^{+\infty} \frac{\mathrm{Im}\{W(\underline{p},\omega^+)\}}{s-\omega^+}\,ds$$

The integration in fact runs only along the branch cut from left to right. Performing the integration, we find

$$\text{A19)} \qquad \mathrm{Re}\{W(\underline{p},\omega^+)\} = (m^{*3}/8\pi^2\hbar^4 p^3)\left((\hbar/m^*)pk_F[(\hbar/m^*)p^2 - 2\omega] + \right.$$

$$\left. + [\omega - (\hbar/m^*)p(\tfrac{1}{2}p-k_F)][\omega - (\hbar/m^*)p(\tfrac{1}{2}p+k_F)]\ln\left|\frac{(\hbar/m^*)p(\tfrac{1}{2}p-k_F)-\omega}{(\hbar/m^*)p(\tfrac{1}{2}p+k_F)-\omega}\right|\right)$$

It should be noted that, for small ω, this just becomes the function $W(\underline{p})$,

where $W(\underline{p})$ is the function which has been found to be responsible for "kinks" in phonon and spin-wave dispersion curves. The nature of the anomolous behavior of $\mathrm{Re}\{W(\underline{p},\omega^+)\}$ in the regions $\omega \sim (\hbar/m^*)p(\frac{1}{2}p-k_F)$ and $\omega \sim (\hbar/m^*)p(\frac{1}{2}p+k_F)$ is determined by the fact that $\mathrm{Im}\{W(\underline{p},\omega)\}$ goes linearly to zero in these regions. For $\omega \sim (\hbar/m^*)p(\frac{1}{2}p-k_F)$, for instance, the important contribution to the integral (A18) comes from the region $s \sim (\hbar/m^*)p(\frac{1}{2}p-k_F)$, where the integrand is approximately

$$\text{A20)} \quad \begin{cases} K\left(\dfrac{s - (h/m^*)p(\frac{1}{2}p-k_F)}{s - \omega^+}\right) & \text{for } (\hbar/m^*)p(\frac{1}{2}p-k_F) < s \\ 0 & \text{for } s < (\hbar/m^*)p(\frac{1}{2}p-k_F) \end{cases}$$

and this region contributes a term

$$\text{A21)} \quad -K[\omega - (\hbar/m^*)p(\tfrac{1}{2}p-k_F)]\ln|\omega - (\hbar/m^*)p(\tfrac{1}{2}p-k_F)|$$

to $\mathrm{Re}\{W(\underline{p},\omega^+)\}$.

We are particularly interested, not in the function $W(\underline{p},\omega^+)$, but in the sum $W(\underline{p},\omega+) + W(\underline{p},-\omega+)$. To find $W(\underline{p},-\omega^+)$ we write

$$\text{A22)} \quad \int_{C'} \frac{W(\underline{p},s)}{s + \omega^+}\, ds = 0 = \oint_{-\infty}^{+\infty} \frac{W(\underline{p},s^-)}{s + \omega^+}\, ds + i\pi W(\underline{p},-\omega^+)$$

where C' is the contour drawn in Fig. A3, and s^- is taken to have a vanishingly small negative imaginary part. Taking real and imaginary parts of this expression yields

$$\text{A23)} \quad \mathrm{Im}\{W(\underline{p},-\omega^+)\} = (1/\pi) \oint_{-\infty}^{+\infty} \frac{\mathrm{Re}\{W(\underline{p},s^+)\}}{s + \omega^+}\, ds$$

$$\mathrm{Re}\{W(\underline{p},-\omega^+)\} = (1/\pi) \oint_{-\infty}^{+\infty} \frac{\mathrm{Im}\{W(\underline{p},s^+)\}}{s + \omega^+}\, ds$$

where advantage has been taken of the relation: $\mathrm{Im}\{W(\underline{p},s^+)\} = -\mathrm{Im}\{W(\underline{p},s^-)\}$.

The analogous equations for $W(\underline{p},\omega^+)$ are, taking real and imaginary parts of Eq. (A17),

$$\text{A24)}\quad \mathrm{Im}\{W(\underline{p},\omega)\} = -(1/\pi)\int_{-\infty}^{+\infty} \frac{\mathrm{Re}\{W(\underline{p},s^+)\}}{s-\omega^+}\,ds$$

$$\mathrm{Re}\{W(\underline{p},\omega)\} = (1/\pi)\int_{-\infty}^{+\infty} \frac{\mathrm{Im}\{W(\underline{p},s^+)\}}{s-\omega^+}\,ds$$

Comparison of (A24) with (A23) yields the following rule for construction of $W(\underline{p},-\omega^+)$ from $W(\underline{p},\omega^+)$: Formally replace ω in the latter function by $-\omega$, and change the sign of the imaginary part. It follows that $\mathrm{Re}\{W(\underline{p},\omega^+) + W(\underline{p},-\omega^+)\}$ is an even function of ω, whereas $\mathrm{Im}\{W(p,\omega^+)+W(\underline{p},-\omega^+)\}$ is odd.

We wish to know the behavior of these functions as functions of $\underline{p}$ for physical values of the frequency, which are, in order of magnitude, $10^{-3}(\hbar k_F^2/m^*)$. Then, except for values of p such that the end of the branch cut falls very near the origin in the ω-plane, we can expand the functions for small ω to get

$$\text{A25)}\quad \mathrm{Im}\{W(\underline{p},\omega^+) + W(\underline{p},-\omega^+)\} = 2\omega\,\frac{\partial}{\partial\omega}\,\mathrm{Im}\{W(\underline{p},\omega^+)\}\Big|_{\omega=0}$$

$$\mathrm{Re}\{W(\underline{p},\omega^+) + W(\underline{p},-\omega^+)\} = 2\,\mathrm{Re}\{W(\underline{p},0)\}$$

These relations hold for all values of p except those for which the quantity $(\hbar k_F/m^*)(p-2k_F)$ is of order ω. But since, for physical values of ω, these values of p are within $10^{-3}k_F$ of $2k_F$, measured spectral properties will in effect be given by

$$\text{A26)}\quad \tfrac{1}{2}\mathrm{Im}\{W(\underline{p},\omega^+) + W(\underline{p},-\omega^+)\} = \omega\begin{cases} m^{*2}/8\pi\hbar^3 p & \text{for } p<2k_F \\ 0 & \text{for } p>2k_F \end{cases}$$

$$\tfrac{1}{2}\mathrm{Re}\{W(\underline{p},\omega^+) + W(\underline{p},-\omega^+)\} = W(\underline{p})$$

where $W(\underline{p})$ is the function already found to be responsible for "kinks" in phonon dispersion curves.

A short summary of the results of this section is in order. We have found the function $W(\underline{p},\omega)$ to have a branch cut on the real axis of the complex ω-plane. The positions of the end points of this branch cut depend parametrically on $\underline{p}$. Near the ends of the branch cut $\mathrm{Im}\{W(\underline{p},\omega^+)\}$ falls off linearly to zero, and remains zero off the branch cut.

By contour integration in the ω-plane, it has been established that $\mathrm{Re}\{W(\underline{p},\omega^+)\}$ has anomalies of the form $(\omega-\omega_o)\ln|\omega-\omega_o|$, where ω_o is the end of a branch cut. It has also been established in this fashion that the functions of physical interest, in cases where frequencies are small, are $\mathrm{Re}\{W(\underline{p},0)\}$ and $\omega\,\partial/\partial\omega\,\mathrm{Im}\{W(\underline{p},\omega^+)\}\big|_{\omega=0}$, and that these functions, considered as functions of $\underline{p}$, display exactly the behavior previously found for anomalies in phonon dispersion curves and phonon lifetime curves.

In particular, we have found that, for $p \sim 2k_F$, the branch cut has one end near the origin of the ω-plane. Near this end of the branch cut, we have

A30) $\mathrm{Im}\{W(\underline{p},\omega^+)\} \simeq K[\omega - (\hbar/m^*)p(\tfrac{1}{2}p-k_F)]$

It then follows that anomalies in the phonon decay rate take the form and magnitude

A31) $$\mathrm{Im}\{W(\underline{p},\omega^+) + W(\underline{p},\omega^+)\} = \begin{cases} K\,\omega & \text{for } p<2k_F \\ 0 & \text{for } p>2k_F \end{cases}$$

and by contour integration it can be established that anomalies in the phonon dispersion curves have form and magnitude

A32) $-K\, v\, (p-2k_F) \ln|p-2k_F|$

where $v = \hbar p/2m^*$ is the velocity of an electron whose wavenumber is $\frac{1}{2}p$.

c. Non-Spherical Fermi Surfaces

In cases where the Fermi surface is not spherical, the anomalous behavior of dispersion curves and lifetimes can still be expected to arise from the behavior of the function

A33) $W^*(\underline{p},\omega^+) = (8\pi^3)^{-1} \int (E_{\underline{k}+\underline{p}} - E_{\underline{k}} - \hbar\omega^+)^{-1} \, d^3k$

where the integral runs over all electron energy states beneath the Fermi surface. This integral may be quite difficult to evaluate for general Fermi surfaces. We show in this section, however, that in the important region near the end of the branch cut in the ω-plane, for small ω, this function has the behavior already observed in the case of a spherical Fermi surface.

The imaginary part of $W^*(\underline{p},\omega^+)$ is given by

A34) $\mathrm{Im}\{W^*(\underline{p},\omega^+)\} = (8\pi^2\hbar)^{-1} \int \delta\,[(E_{\underline{k}+\underline{p}} - E_{\underline{k}})/\hbar - \omega]\, d^3k$

This integral runs over the surface R in $\underline{k}$ space defined, for fixed $\underline{p}$ and ω, by

A35) $E_{\underline{k}+\underline{p}} - E_{\underline{k}} - \hbar\omega = 0$

The behavior of $\mathrm{Im}\{W^*(\underline{p},\omega^+)\}$, in the important regions near the ends of the branch cut of $W^*(\underline{p},\omega)$, is determined by the shape of the surface R for values of ω which make R nearly tangent to the Fermi surface. Inspection of Fig. A4 indicates that, for $\underline{p}$ in such a direction that R becomes tangent to a convex part of the Fermi surface, the imaginary part of

$W^*(\underline{p},\omega^+)$ will indeed fall off linearly to zero as ω approaches the branch point. The behavior found in the spherical case should then be repeated in this case, for $\underline{p}$ in proper directions.

We proceed to find an expression for $W^*(\underline{p},\omega^+)$ when ω is near the end of the branch cut, for such $\underline{p}$ that the region of tangency occurs where the Fermi surface is convex and for small ω. It will be convenient to consider the properties of the constant energy surfaces in the $\underline{p}$ direction, since we shall find that R becomes tangent to the Fermi surface in this direction. In the vicinity of the point $-\frac{1}{2}\underline{p}$, as indicated in Fig. A5, we can write $E_{\underline{k}}$ in the form*

A36) $$E_{\underline{k}} \simeq E_{\frac{1}{2}\underline{p}} + a(k_1+\tfrac{1}{2}p_1) + b(k_2+\tfrac{1}{2}p_2)^2 + c(k_3+\tfrac{1}{2}p_3)^2$$

where k_1 is the component of $\underline{k}$ normal to the surface $E_{\underline{k}} = E_{\frac{1}{2}\underline{p}}$ at the point $-\frac{1}{2}\underline{p}$, and the directions of k_2 and k_3 have been chosen to eliminate cross terms in k_2k_3 from Eq. (A34). We can likewise write

A37) $$E_{\underline{k}+\underline{p}} \simeq E_{\frac{1}{2}\underline{p}} - a(k_1+\tfrac{1}{2}p_1) + b(k_2+\tfrac{1}{2}p_2)^2 + c(k_3+\tfrac{1}{2}p_3)^2$$

so the defining equation for the surface R becomes

A38) $$-2a(k_1+\tfrac{1}{2}p_1) - \hbar\omega = 0$$

The branch cut then has its end for small ω when $\underline{p}$ is in the vicinity of $2\underline{k}_o$, where $\underline{k}_o$ is the vector on the Fermi surface in the $\underline{p}$ direction. For such $\underline{p}$, the imaginary part of $W^*(\underline{p},\omega^+)$ is given by

A39) $$\mathrm{Im}\{W^*(\underline{p},\omega^+)\} \simeq (A/8\pi^2\hbar) \int \delta\,[(2a/\hbar)(k_1+\tfrac{1}{2}p_1) + \omega]\; dk_1$$

where A is the area intersected by the Fermi surface on the surface R.

---

*Inversion symmetry has been assumed of the Fermi surface.

The equation of the Fermi surface near the point $-\frac{1}{2}\underline{p}$ is

A40) $$E_F \simeq E_{\frac{1}{2}\underline{p}} + a(k_1+\tfrac{1}{2}p_1) + b(k_2+\tfrac{1}{2}p_2)^2 + c(k_3+\tfrac{1}{2}p_3)^2$$

The area intersected on R is thus elliptical in shape, and the area A is

A41) $$A = \pi(bc)^{-\frac{1}{2}}\,(E_F - E_{\frac{1}{2}\underline{p}} + \tfrac{1}{2}\hbar\omega) =$$

$$= \tfrac{1}{2}\pi\hbar(bc)^{-\frac{1}{2}}\,[(2a\,\cos\theta)(\tfrac{1}{2}p-k_o)/\hbar + \omega]$$

where θ is the angle between the k_1 and $\underline{p}$ directions. Then the imaginary part of $W^*(\underline{p},\omega^+)$ is

A42) $$\mathrm{Im}\{W^*(\underline{p},\omega^+)\} = \begin{cases} \dfrac{\hbar}{32\pi a(bc)^{\frac{1}{2}}}\ [\omega - (2a\,\cos\theta)(\tfrac{1}{2}p-k_o)/\hbar] & \\ \qquad\qquad \text{— for } (2a\,\cos\theta)(\tfrac{1}{2}p-k_o)/\hbar < \omega & \\ 0 \qquad\qquad \text{for } \omega < (2a\,\cos\theta)(\tfrac{1}{2}p-k_o)/\hbar & \end{cases}$$

The constants a, b and c have simple physical interpretation. The ratios (a/2b) and (a/2c) are, respectively, the radii of curvature R_1 and R_2 of the surface $E_k = E_{\frac{1}{2}\underline{p}}$ at the points $\pm\frac{1}{2}\underline{p}$. The constant a can be interpreted by noting that

A43) $$\underline{v} = \hbar^{-1}\,\nabla_{\underline{k}}\,E_{\underline{k}}\,\Big|_{\underline{k}=-\frac{1}{2}\underline{p}} = \underline{n}\,(a/\hbar)$$

where $\underline{v}$ is the velocity of an electron whose wave vector is $-\frac{1}{2}\underline{p}$. The vector $\underline{n}$ is the unit vector normal to the surface $E_{\underline{k}} = E_{\frac{1}{2}\underline{p}}$ at the point $-\frac{1}{2}\underline{p}$.

From Eq. (A42), using the results of Sec. b, we see that the phonon decay rate can be expected to display anomalies of form and magnitude

A44) $\mathrm{Im}\{W^*(\underline{p},\omega^+) + W^*(\underline{p},-\omega^+)\} = \begin{cases} K\,\omega & \text{for } p<2k_o \\ 0 & \text{for } p>2k_o \end{cases}$

where

A45) $K = (R_1R_2)^{\frac{1}{2}}/4\pi\hbar v^2$

and the anomalies of the phonon dispersion curves will have form and magnitude

A46) $-K\,v\cos\theta\,(p-2k_o)\ln|p-2k_o|$.

APPENDIX 2

The Electron-Ion Matrix Element in Aluminum

Bardeen's calculation of the matrix element $(\underline{k}+\underline{p}|\nabla V(\underline{r})|\underline{k})$ uses the basic assumption that the electron wave functions, written in the Bloch form $u_{\underline{k}}(\underline{r})\, e^{i\underline{k}\cdot\underline{r}}$, can be approximated as $u_o(\underline{r})\, e^{i\underline{k}\cdot\underline{r}}$, where $u_o(\underline{r})$ is the lowest eigenfunction of the conduction electron Hamiltonian. This assumption is, presumably, valid for monovalent metals; we shall attempt to show here that it can be replaced by two other assumptions: that the electron wave functions can be adequately represented by single Orthogonalized Plane Waves (OPW),[17] and that each ion core is well confined within its own unit cell.

This replacement of Bardeen's assumption is possible because the assumption has been used only to determine the properties of $u_{\underline{k}}(\underline{r})$ in the vicinity of the unit cell wall. The important properties are, first, that $u_{\underline{k}}(\underline{r})$ should have spherical symmetry in this region, and second, that $u_{\underline{k}}(r_s)$ should not vary much with $\underline{k}$. The OPW are constructed by adding to plane waves linear combinations of ion core wavefunctions (with coefficients so chosen as to make the OPW orthogonal to all core states.) For ions which are well confined within their own unit cells, then, the OPW necessarily have almost pure plane wave character near the cell wall. Then $u_{\underline{k}}(\underline{r})$ will have spherical symmetry in this region, and will in fact be very nearly flat. The value $u_{\underline{k}}(r_s)$ will depend on $\underline{k}$ only through a normalization constant. If the largest ion core

wavefunction falls off as $e^{-r/a}$, then the natural parameter for a power series expansion of the normalization constant is $(ka)^2$. From Froese's[18] calculations for the trivalent aluminum ion, for instance, we find $k_F a = 1/5$, so the variation of $u_{\underline{k}}(r_s)$ will be small for $\underline{k}$ in the region of interest. (It is also desirable, though of less importance, that the number C in Eq. (I,23) be independent of $\underline{k}$. C is proportional to the second derivative $\partial^2 u_{\underline{k}}(\underline{r})/\partial r^2$, evaluated at the cell wall. This quantity will be quite small if the single OPW assumption is justified, since it falls off with distance in the same way as the core wavefunctions. If a power series expansion is made, the parameter is $ka = k/5k_F$, so the variation with k should be reasonably slow.)

Bardeen's calculation of the electron-ion matrix element therefore goes through under our assumptions. The question of whether the single-OPW approximation is good for any particular metal is rather difficult to answer, but the work of Heine[17] shows rapid convergence, in aluminum, for the expansion of the Bloch functions in single OPW's.

APPENDIX 3

Competing Decay Processes for Phonons

a. Three-Phonon Effects

Terms in the potential energy of the lattice which are cubic in the ionic displacements give rise to phonon-phonon interactions. These interactions contribute to the phonon decay rate, and can be expected to reduce, to some extent, the relative importance of electron-phonon effects. We show here that this reduction is not serious, estimating the decay rate from phonon-phonon interactions by using a phenomenological treatment due to Klemens.[19]

The cubic terms in the lattice Hamiltonian can be written in second quantization as terms cubic in the phonon field operators. If only one phonon is initially present in the lattice, having wave number $\underline{q}$ and polarization $\underline{e}$, the only cubic terms in the Hamiltonian capable of destroying the phonon are

$$A47) \quad H' = \Sigma_{\underline{k},\underline{p};\underline{s},\underline{t}} \, C(\underline{k},\underline{p},\underline{q};\underline{s},\underline{t},\underline{e}) \, a^{*}_{\underline{k},\underline{s}} \, a^{*}_{\underline{p},\underline{t}} \, a_{\underline{q},\underline{e}}$$

where $a^{*}_{\underline{q},\underline{e}}$ and $a_{\underline{q},\underline{e}}$ are, respectively, the operators which create and destroy phonons of wavenumber $\underline{q}$ and polarization $\underline{e}$. These operators have the matrix elements[19]

$$A48) \quad (n' \mid a \mid n) = [\hbar n/2M\omega]^{\frac{1}{2}} \, \delta_{n',n-1}$$

$$(n' \mid a^{*} \mid n) = [\hbar(n+1)/2M\omega]^{\frac{1}{2}} \, \delta_{n',n+1}$$

where the polarization and wavenumber subscripts have been suppressed.

We follow Klemens in taking

$$A49)\quad C(\underline{k},\underline{p},\underline{q};\underline{s},\underline{t},\underline{e}) = \frac{-2i\gamma\omega_{\underline{k},\underline{s}}\,\omega_{\underline{p},\underline{t}}\,\omega_{\underline{q},\underline{e}}}{(3N^3)^{\frac{1}{2}}\,v_{\underline{q},\underline{e}}} \sum_{\underline{R}} e^{-i(\underline{k}+\underline{p}-\underline{q})\cdot\underline{R}}$$

where $\gamma \sim 2$, $v_{\underline{q},\underline{e}}$ is the phase velocity of the phonon initially present, and the sum runs over the Bravais lattice.

The transition probability for decay of one phonon into all possible pairs of phonons is, in the Debye approximation,

$$A50)\quad W = \frac{\gamma^2\hbar^2\Omega}{24\pi^2MN} \sum_{\underline{s},\underline{t}} (c_{\underline{s}}c_{\underline{t}}/c_{\underline{e}})\, q \sum_{\underline{K}} \int k\,|\underline{k}-\underline{K}-\underline{q}|\ \delta(\hbar c_{\underline{s}}k + \hbar c_{\underline{t}}\,|\underline{k}-\underline{K}-\underline{q}| - \hbar c_{\underline{e}}q)\, d^3k$$

where the integral goes over the Brillouin zone, and $c_{\underline{s}}$ is the sound velocity of the phonon whose polarization is $\underline{s}$. The integral in Eq. (A50) can be done rather conveniently, if the Brillouin zone is taken to be a sphere of radius q_o, in the coordinates u, v, φ, where[20]

$$A51)\quad u = \tfrac{1}{2}(k + |\underline{k}-\underline{K}-\underline{q}|)$$

$$v = \tfrac{1}{2}(k - |\underline{k}-\underline{K}-\underline{q}|)$$

and φ is the azimuthal angle about $\underline{K}+\underline{q}$. In these coordinates the transition probability becomes

$$A52)\quad W = \frac{\gamma^2\hbar\Omega}{6\pi MN}\, q \sum_{\underline{s},\underline{t}} (c_{\underline{s}}c_{\underline{t}}/c_{\underline{e}}) \sum_{\underline{K}} \frac{1}{|\underline{K}+\underline{q}|} \iint (u^2-v^2)^2\, \delta(au + bv - cq)\, du\, dv$$

where

$$A53)\quad a = c_{\underline{s}} + c_{\underline{t}} \quad ; \quad b = c_{\underline{s}} - c_{\underline{t}}$$

and the integral runs over the area of the u,v plane which is shaded in Fig. A6. The δ-function insures that in fact this integral shall go over only the line drawn dashed in Fig. A6.

The two polarization branches require six different decay processes to be distinguished, which we investigate individually. Each of these processes is characterized by values of c/a and b/a. Since the function $\frac{1}{2}|\underline{K}+\underline{q}|$ has the value $\frac{1}{2}q$ for $\underline{K}=0$ and minimum value $\frac{1}{2}K-\frac{1}{2}q$ for $\underline{K}\neq 0$, it is possible to know from Fig. A6 and the values of c/a and b/a, whether for given $\underline{K}$ a process makes any contribution to the transition probability. We take the longitudinal sound velocity to be twice the transverse sound velocity, and we symbolize by $\underline{l \rightarrow l+t}$ the process in which a longitudinal phonon decays into one longitudinal and one transverse phonon. The six decay processes are

i) $\underline{t \rightarrow l+l}$ Here the dashed line in Fig. A6 lies entirely outside the area of integration, since $cq/a=\frac{1}{4}q$ and $b/a=0$. This result is independent of the value of $\underline{K}$, so this process makes no contribution.

ii) $\underline{t \rightarrow l+t}$ Here again the dashed line falls outside the area of integration for all $\underline{K}$, since $cq/a=q/3$ and $b/a=1/3$.

iii) $\underline{t \rightarrow t+t}$ Here the dashed line is the line $u=\frac{1}{2}q$. For $\underline{K}=0$ we get a contribution, but for $\underline{K}\neq 0$ there is none.

iv) $\underline{l \rightarrow l+l}$ The considerations here are the same as in process (iii).

v) $\underline{l \rightarrow l+t}$ Here the dashed line falls inside the area of integration for $\underline{K}=0$, and, with some values of $\underline{q}$, also for $\underline{K}$ one of the shortest reciprocal lattice vectors (of magnitude $2q_o$.) The values of $\underline{q}$ which give contributions for $\underline{K}\neq 0$ can be seen to lie outside the sphere of radius $2q_o/3$, since $cq/a=2q/3$ and $b/a=1/3$.

vi) $\underline{l \rightarrow t+t}$ This process also contributes for $\underline{K}=0$ and, with $q>2q_o/3$,

for $\underline{K}$ the shortest reciprocal lattice vectors, since cq/a=q and b/a=0.

In view of the above survey, we compute the transition probability for $q<2q_o/3$, where only processes (iii), (iv), (v), and (vi) contribute, and these only for $\underline{K}=0$. Except in process (v) both final phonons lie on the same polarization branch, and the integral in Eq. (A52) becomes

A54) $$\iint(u^2-v^2)^2\delta(u-cq/a)\,du\,dv = q^5\,[(c/a)^4 - (c/a)^2/6 + 1/80]$$

for $q<2q_o/3$. For processes (iii) and (iv) $c/a=\frac{1}{2}$, and the integral takes the value $q^5/30$. For process (vi) c/a = 1, and the integral takes on a value twenty-five times as large. In process (iv), the only remaining contributor, the integral in Eq. (A52) becomes

A55) $$\iint(u^2-v^2)^2\delta(u+bv/a-cq/a)\,du\,dv \cong q^5/60\ .$$

The most important contribution apparently comes from process (vi) and, including only this process we get, for constants corresponding to aluminum,

A56) $$W/\omega \cong 0.06\,(q/q_o)^4$$

Reference to Fig. 4 shows that this decay rate is quite small compared to the decay rate from electron-phonon interaction, becoming comparable only near the boundary of the Brillouin zone.

For transverse phonons, the only decay mechanism is process (iii), so the decay rate will be twenty-five times smaller.

b. Two-Pair Creation

One possibly important phonon decay process can be described as follows: the phonon excites an electron-hole pair, and the excited

electron, without falling back beneath the Fermi sea, subsequently excites a second pair through electron-electron interaction. Since energy conservation is not necessary in the intermediate state, the restrictions which might cause a break for phonons of wave number $2k_F$ do not exist; so if this process contributes significantly to the phonon decay rate it will partially mask out the effects which interest us. We estimate the decay rate for this process here, however, and show that it is much smaller than the decay rate into single electron-hole pairs.*

We reconsider shortly, first, the decay rate from single pair creation. This decay rate can be calculated as a transition probability for the whole system, from the state with the electron gas in its ground state and one phonon present to the state with one electron-hole pair excited and the phonon absent. We represent this process pictorially in Fig. A7, taking account of momentum conservation. The transition probability is given by

$$A57) \quad W_1 = (1/8\pi^3\hbar)(N/\Omega)\Sigma_{\underline{K}} \int d^3k \; |v_p(\underline{q}+\underline{K})|^2 \; \delta(E_{\underline{k}+\underline{q}+\underline{K}} - E_{\underline{k}} - \hbar\omega)$$

where $v_p(\underline{q}+\underline{K})$ is the matrix element of the electron-phonon interaction between the initial and final states, and is given by

$$A58) \quad v_p(\underline{q}) = (\underline{e}\cdot\underline{q}) \frac{4\pi e^2}{q^2+a^2} (\hbar/2M\omega)^{\frac{1}{2}}$$

---

*Such a two-step decay can occur by several different processes, each of which will contribute to the two-pair decay rate a term of the same order as the term estimated here.

where the Thomas-Fermi approximation has been used for the effect of electron shielding. The integration on $\underline{k}$ is restricted, since the final state must have an electron and a hole, to the region of $\underline{k}$ space defined by

A59) $$k<k_F$$

$$|\underline{k}+\underline{q}+\underline{K}|>k_F$$

and since the energy conserving δ-function can be written

A60) $$\delta(E_{\underline{k}+\underline{q}+\underline{K}} - E_{\underline{k}} - \hbar\omega) = (m^*/\hbar^2)\delta[\underline{k}\cdot(\underline{q}+\underline{K}) + \tfrac{1}{2}(\underline{q}+\underline{K})^2 - m^{*2}\omega/\hbar]$$

the region available for the integration on $\underline{k}$ is just that indicated in Fig. A8, which should be imagined as rotated about the vector $\underline{q}+\underline{K}$. The unshaded volume is forbidden by the electron-hole requirement, and energy conservation requires that $\underline{k}$ lie in a plane perpendicular to $\underline{q}+\underline{K}$, and a distance $-\frac{1}{2}|\underline{q}+\underline{K}| + m^*\omega/\hbar|\underline{q}+\underline{K}|$ along the $\underline{q}+\underline{K}$ direction. (Since $m^*\omega/\hbar k_F^2 \sim 10^{-3}$, this distance is almost $-\frac{1}{2}|\underline{q}+\underline{K}|$.) The plane is indicated by the dashed line in Fig. A8. $\underline{k}$ then lies on a ring, whose area is

A61) $$A = \pi[k_F^2 - (\tfrac{1}{2}|\underline{q}+\underline{K}| - m^*\omega/\hbar|\underline{q}+\underline{K}|)^2] - \pi[k_F^2 - (\tfrac{1}{2}|\underline{q}+\underline{K}| + m^*\omega/\hbar|\underline{q}+\underline{K}|)^2] =$$

$$= 2\pi m^*\omega/\hbar$$

The integration over the δ-function introduces a factor $|\underline{q}+\underline{K}|^{-1}$. The result for W_1, then, estimating that about 10 reciprocal lattice vectors enter into the sum and giving $|\underline{q}+\underline{K}|$ the value $2k_F$, is

A62) $$W_1 \simeq (5N/4\pi^2\Omega)|v_p(2k_F)|^2 (m^{*2}/\hbar^4 k_F)\omega \simeq 10^{-2}\omega$$

The two-pair creation is illustrated in Fig. A9, with the electron-electron interaction represented by a dashed line carrying momentum $\hbar\underline{n}$.

The transition probability for this process can be written

$$A63)\quad W_2 = (1/8\pi^3)\,\Sigma_K (N/\hbar\Omega)\int d^3n \int d^3k \int d^3p \lim_{\eta\to 0} \frac{|v_p(\underline{q}+\underline{K})|^2 |v_e(\underline{n})|^2}{|E_{\underline{k}+\underline{q}+\underline{K}} - E_{\underline{k}} - \hbar(\omega+i\eta)|^2} \times$$

$$\times \quad \delta(E_{\underline{k}+\underline{q}+\underline{K}-\underline{n}} - E_{\underline{k}} + E_{\underline{p}+\underline{n}} - E_{\underline{p}} - \hbar\omega)$$

where the pole of the integrand has been treated as directed by Schiff.[21] $v_e(\underline{n})$ is the matrix element of the (screened) electron-electron interaction between intermediate and final states, given by

$$A64)\quad v_e(\underline{n}) = \frac{4\pi e^2}{n^2+a^2} \qquad ;\quad v_e(2k_F) \simeq 3\, v_p(2k_F) \text{ for aluminum}$$

for Thomas-Fermi screening.

Requiring that the final state contain two electron-hole pairs restricts the sums on $\underline{k}$ and $\underline{p}$ by

$$A65)\qquad k<k_F \qquad\qquad p<k_F$$

$$|\underline{k}+\underline{q}+\underline{K}-\underline{n}| > k_F \qquad\qquad |\underline{p}+\underline{n}| > k_F$$

The energy differences $E_{\underline{k}+\underline{q}+\underline{K}-\underline{n}} - E_{\underline{k}}$ and $E_{\underline{p}+\underline{n}} - E_{\underline{p}}$ must both be positive, so each must be smaller than or equal to $\hbar\omega$. We take advantage of this fact by writing

$$A66)\quad \delta(E_{\underline{k}+\underline{q}+\underline{K}-\underline{n}} - E_{\underline{k}} + E_{\underline{p}+\underline{n}} - E_{\underline{p}} - \hbar\omega) =$$

$$= (m^{*2}/\hbar^3)\int_0^{\omega} \delta[\underline{k}\cdot(\underline{q}+\underline{K}-\underline{n}) + \tfrac{1}{2}(\underline{q}+\underline{K}-\underline{n})^2 - m^*s/\hbar]\,\delta[\underline{p}\cdot\underline{n} + \tfrac{1}{2}n^2 - m^*(\omega-s)/\hbar]\,ds$$

where the limits on the s integration are required by the necessity for positive energy differences.

The regions available for the $\underline{p}$ and $\underline{k}$ integrations are shown in Fig. A10. The area allowed for $\underline{p}$, for fixed s, is just $2\pi m^*(\omega-s)/\hbar$, and a factor n^{-1} is introduced by integration over the δ-function. Performing the $\underline{p}$ and s integrations then gives a factor

$$\text{A67)} \quad \begin{cases} (2\pi/n)\{\omega-(\hbar/m^*)[\underline{k}\cdot(\underline{q}+\underline{K}-\underline{n}) + \tfrac{1}{2}(\underline{q}+\underline{K}-\underline{n})^2]\} & \text{for } 0<(\hbar/m^*)[\underline{k}\cdot(\underline{q}+\underline{K}-\underline{n})+\tfrac{1}{2}(\underline{q}+\underline{K}-\underline{n})^2]<\omega \\ 0 & \text{otherwise} \end{cases}$$

The $\underline{k}$ integration is thus confined to the ring, of triangular cross section, indicated by the blackened area in Fig. A10.

The reason for the smallness of W_2 has now become apparent. Barring bad behavior of the squared energy denominator in Eq. (A63), integration over $\underline{k}$ would give a momentum-space factor ω^3, and since only phonon energies and electron energies enter the problem, we would expect W_2 to be of the order of magnitude $(\hbar\omega/E_F)^2\omega$. In fact we now investigate the behavior of the energy denominator, and show that it can be expected to introduce, at worst, a factor of order $(E_F/\hbar\omega)$, so that W_2 still remains small in comparison to W_1.

We can write the squared energy denominator in Eq. (A63) as

$$\text{A68)} \quad \frac{1}{|E_{\underline{k}+\underline{q}+\underline{K}}-E_{\underline{k}}-\hbar(\omega+i\eta)|^2} = \frac{m^*}{2i\eta\hbar^3}\left(\frac{1}{\underline{k}\cdot(\underline{q}+\underline{K})+\frac{1}{2}(\underline{q}+\underline{K})^2-m\,(\omega+i\eta)/\hbar} + \right.$$
$$\left. - \frac{1}{\underline{k}\cdot(\underline{q}+\underline{K})+\frac{1}{2}(\underline{q}+\underline{K})^2-m^*(\omega-i\eta)/\hbar}\right)$$

This denominator behaves badly only for values of $\underline{n}$ for which the allowed region of the $\underline{k}$ integration intersects the plane, indicated by a dotted line in Fig. A10, on which the energy denominator becomes zero. For

such values of $\underline{n}$, neglecting for the moment the shape of the integration volume and the variation of factors in the numerator, integration over k_1, the component of $\underline{k}$ parallel to $\underline{q}+\underline{K}$, gives

$$\text{A69)}\quad (m^*/2i\eta\hbar^3|\underline{q}+\underline{K}|)\left[\ln\left(\frac{(k_{1max}+\frac{1}{2}|\underline{q}+\underline{K}|)|\underline{q}+\underline{K}| - m^*(\omega+i\eta)/\hbar}{m^*(\omega+i\eta)/\hbar}\right) + \ln\left(\frac{(k_{1max}+\frac{1}{2}|\underline{q}+\underline{K}|)|\underline{q}+\underline{K}| - m^*(\omega+i\eta)/\hbar}{m^*(\omega+i\eta)/\hbar}\right)\right]$$

since the minimum value of k_1 is $-\frac{1}{2}|\underline{q}+\underline{K}|$. There is no contribution from either limit from the real parts of the logarithms. The imaginary parts of the logarithms contribute, in the limit $\eta \to 0$, a factor

$$\text{A70)}\quad (m^*/\hbar^3|\underline{q}+\underline{K}|)\{1/\omega \quad -m^*/[\hbar|\underline{q}+\underline{K}|(k_{1max}+\tfrac{1}{2}|\underline{q}+\underline{K}|)]\}$$

the second term being negligible in comparison with the first. The simplest procedure available to us at this point, then, will be to overestimate the effect of the squared energy denominator by giving it the value $(m^*/\hbar^3|\underline{q}+\underline{K}|^2\omega)$.

The allowed volume for the $\underline{k}$ integration is just $m^{*2}\omega^2/\hbar^2|\underline{q}+\underline{K}-\underline{n}|$, and the function given in (A67) has the average value $\pi\,\omega/n$ over this volume. The integration on $\underline{n}$ can be approximated by giving n and $|\underline{q}+\underline{K}-\underline{n}|$ the value $2k_F$, and since the n integration cuts off at $n=2k_F$ the integration volume is $32\pi k_F^3/3$. The range of the reciprocal lattice sum here is $|\underline{q}+\underline{K}|<4k_F$, so about 80 terms can be expected to enter into this sum. The final result is

$$\text{A71)}\quad W_2/W_1 < \frac{m^{*3}\omega}{10\pi^4\hbar^5}\,|v_e(2k_F)|^2 \approx 10^{-4}$$

so the decay rate from two-pair creation can be neglected in comparison to the decay rate from single pair creation.

APPENDIX 4

Images in Spin-Wave Spectra of Antiferromagnets

The negative spin-wave "dispersion curve" of Fig. 6 implies that, for the model used, the assumption of a ferromagnetic ground state is not justified. Rather, it implies that the ground state of the spin system should be an antiferromagnetic spiral structure, whose pitch can be deduced from the position of the minimum in the negative dispersion curve.[13,22,23] The extreme sensitivity of our results to small changes in the position of the Fermi surface assures that these comments should not be assigned more than a speculative significance, but it is interesting to note that the rare earths do display spiral structure at somewhat elevated temperatures.[24] It may be that the sensitivity of the dispersion curves (suggested, in fact, by the disparity between the two curves of Fig. 6) can help to explain some of the remarkable magnetic properties of the rare earths.[24]

The results of Part II are applicable to rare earth metals only when in a ferromagnetic state, either naturally, or under the influence of a strong magnetic field.[24] For spiral antiferromagnetic spin arrangements on Bravais lattices, Kasuya[13] as well as Yosida[23] has found a spin wave spectrum given by

$$\text{A72)} \quad \{[d - I(\underline{q}) + I(\underline{q}_o)][I(\underline{q}) - \tfrac{1}{2} I(\underline{q}_o+\underline{q}) - \tfrac{1}{2} I(\underline{q}_o-\underline{q})]\}^{\frac{1}{2}}$$

where d is a constant used to describe anisotropy energy in the hard direction of magnetization, and $I(\underline{q})$ is proportional to our $\Sigma_{\underline{K}}(W(\underline{q}+\underline{K})-W(\underline{K}))$.

$\underline{q}_o$ gives the pitch of the ground-state spiral structure. Eq. (A59) indicates that in the spin-wave spectra of antiferromagnetic structures images of the Fermi surface will appear, with magnitude comparable to the magnitude they have for ferromagnets. The condition for a kink is that $\underline{q}$ satisfy one of the conditions

A73) $$|\underline{q} + \underline{K}| = 2k_F$$

$$|\underline{q} \pm \underline{q}_o + \underline{K}| = 2k_F \, .$$

REFERENCES

1. P-G. de Gennes and J. Friedel, J. Phys. Chem. Solids 4, 71 (1958).
2. W. Kohn, Phys. Rev. Letters 2, 393 (1959).
3. E. J. Woll and S. J. Nettel, Phys. Rev. 123, 796 (1961).
4. B. N. Brockhouse, K. R. Rao and A. D. B. Woods, Phys. Rev. Letters 7, 93 (1961).
5. J. Bardeen, Phys. Rev. 52, 688 (1937).
6. J. S. Langer and S. H. Vosko, J. Phys. Chem. Solids 12, 196 (1959).
7. These calculations were performed by Dr. Vosko at the I.B.M. 650 Computer installation of the Carnegie Institute of Technology.
8. J. Bardeen and D. Pines, Phys. Rev. 99, 1140 (1955).
9. The author is indebted to Dr. Vosko for this remark.
10. A. B. Pippard, Phil. Mag. 46, 1104 (1955).
11. M. A. Ruderman and C. Kittel, Phys. Rev. 96, 99 (1954).
12. P-G. de Gennes, Compt. rend. 247, 1836 (1958).
13. T. Kasuya, Progr. Theoret. Phys. (Kyoto) 16, 58 (1956).
14. T. Holstein and H. Primakoff, Phys. Rev. 58, 1098 (1940).
15. S. H. Liu, Phys. Rev. 121, 451 (1961).
16. J. Van Kranendonk and J. H. Van Vleck, Revs. Modern Phys. 30, 1 (1958).
17. V. Heine, Proc. Roy. Soc. (London) A240, 340 (1957).
18. C. Froese, Proc. Cambridge Philosophical Soc. 53, 206 (1957).
19. P. G. Klemens, Solid State Physics, edited by F. Seitz and D. Turnbull (Academic Press, Inc., New York, 1958), pp. 7-27.

20. H. Margenau and G. M. Murphy, The Mathematics of Physics and Chemistry (D. Van Nostrand Company, Inc., New York, 1943), p. 177.

21. L. I. Schiff, Quantum Mechanics (McGraw-Hill Book Company, Inc., New York, 1955), pp. 202-205.

22. J. Villain, J. Phys. Chem. Solids 11, 303 (1959).

23. K. Yosida and H. Miwa, Technical Report of Institute for Solid State Physics, Ser. A, No. 14, University of Tokyo, Tokyo, Japan (unpublished).

24. B. L. Rhodes, S. Levgold, and F. H. Spedding, Phys. Rev. 109, 1547 (1958). See also W. C. Kohler et al, Rare Earth Research Developments Conference, University of California, Lake Arrowhead, California (unpublished), Sec. II.

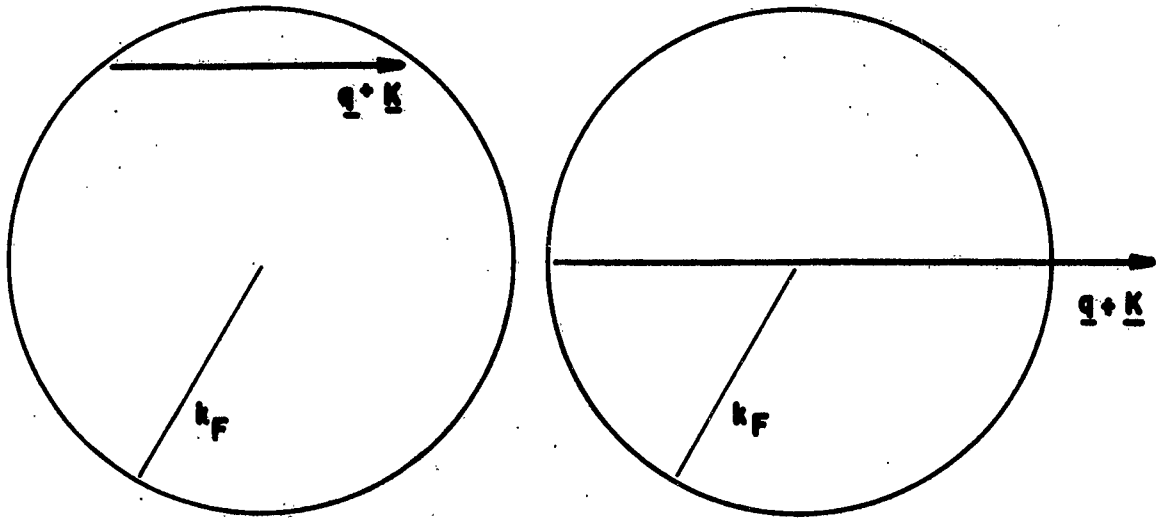

FIGURE 1

Virtual pair excitation for the cases $|\underline{q}+\underline{K}|<2k_F$ and $|\underline{q}+\underline{K}|>2k_F$.

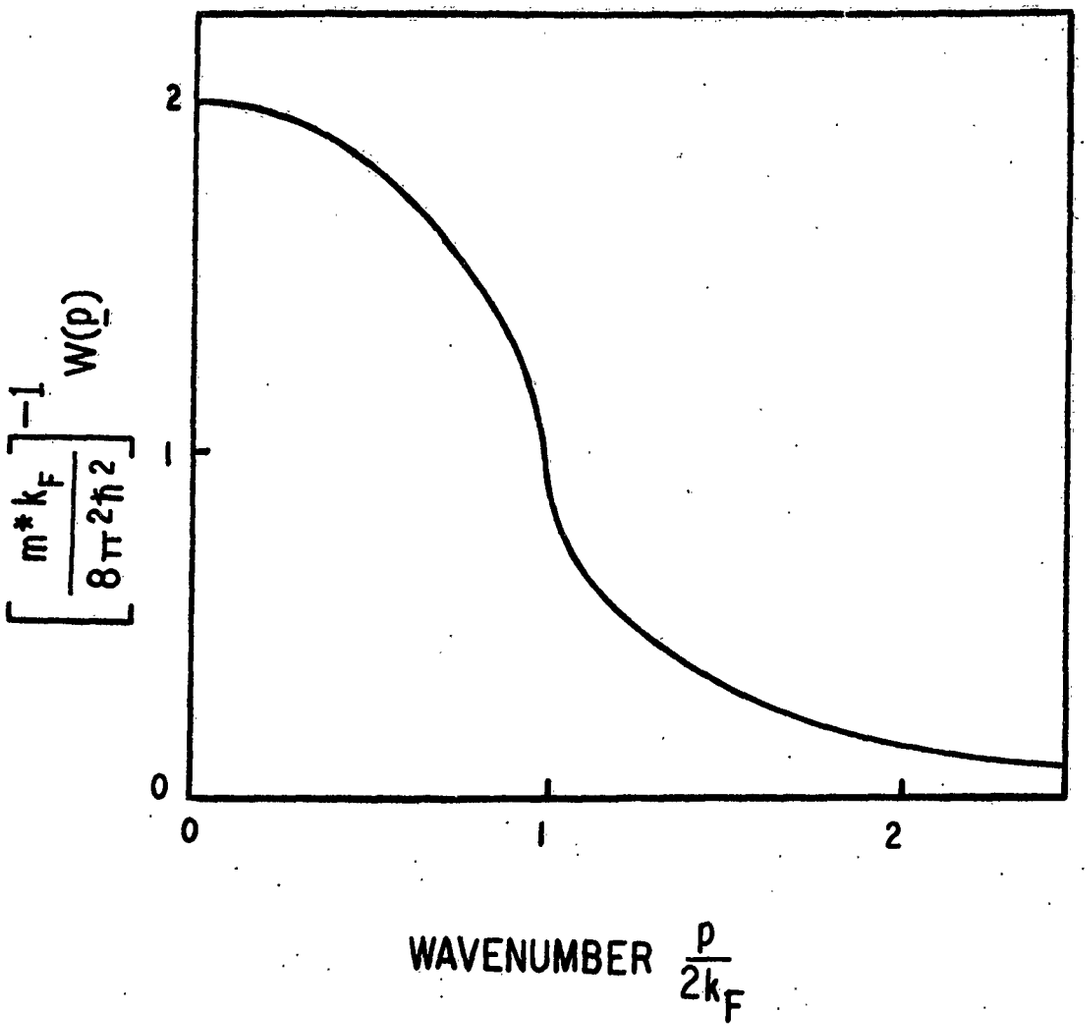

FIGURE 2

Plot of the function W(p). Note infinite slope at $p=2k_F$.

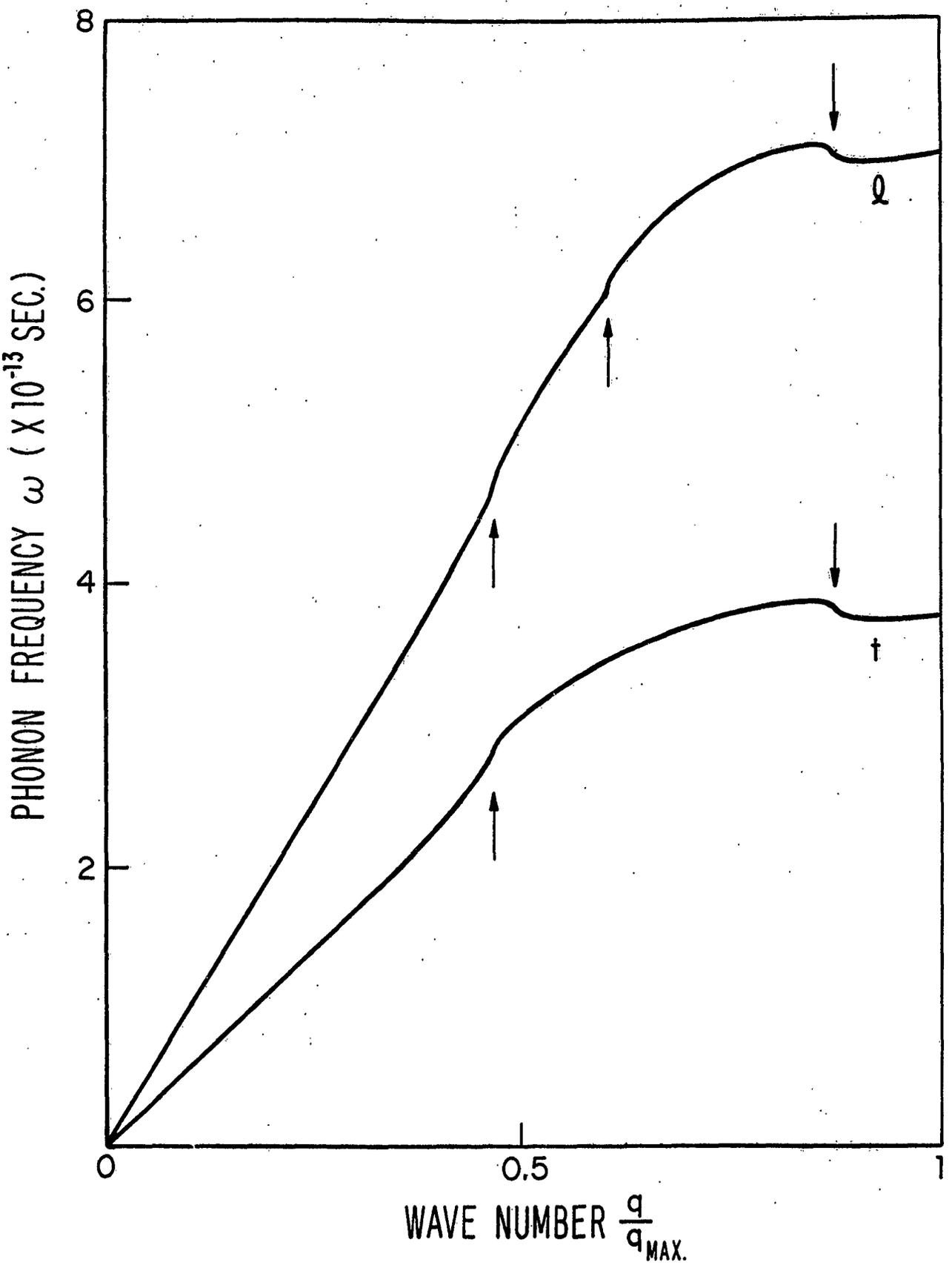
8
6
4
2
0
0.5
1
PHONON FREQUENCY ω (X 10⁻¹³ SEC.)
WAVE NUMBER q/q_MAX.
l
t

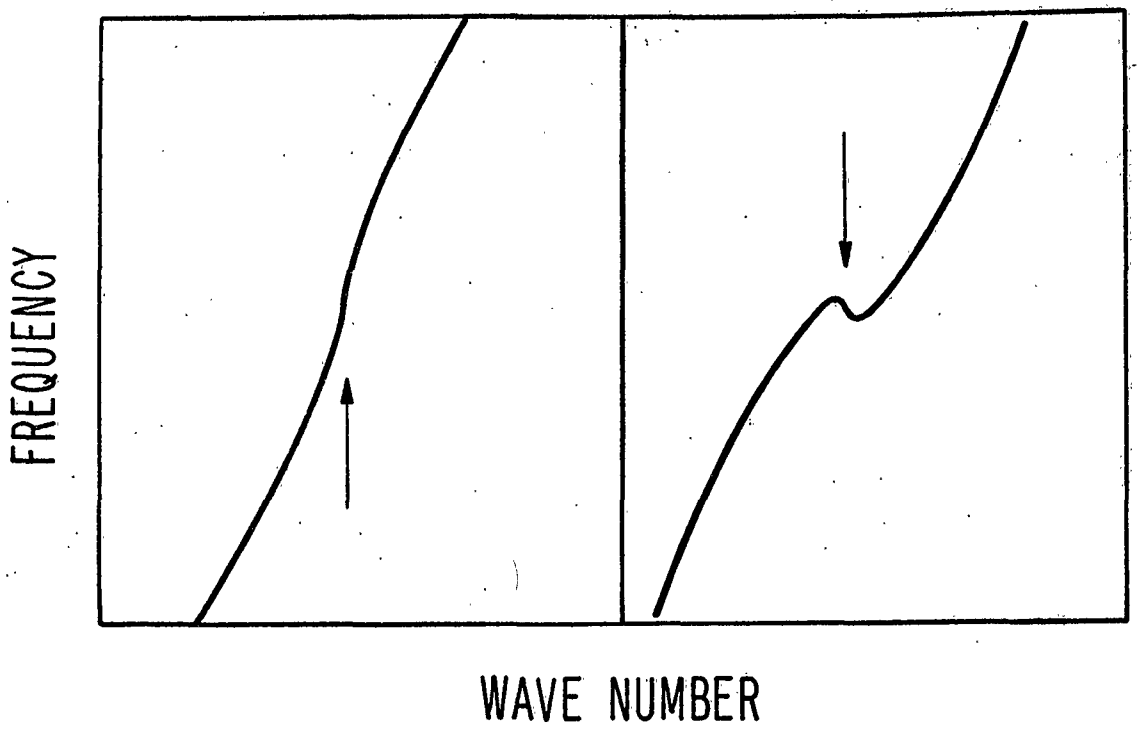

FIGURE 3a (previous page)

Dispersion curves calculated from the Uniform Electron Gas Model for constants corresponding to aluminum. These curves are for the (111) direction of reciprocal space; "ℓ" and "t" refer to longitudinal and transverse directions of polarization. Fermi surface images are indicated by arrows. While the considerations of Sec. B suggest that the model used is inappropriate for aluminum, kinks of this general order may well appear in other cases.

FIGURE 3b (above)

Characteristic "upward" and "downward" anomalies of the dispersion curves. Scales are enlarged five times from the scales of Fig. 3a. While no simple downward anomaly occurs in the case of aluminum, the example shown here should be helpful in interpretation of such anomalies where they do appear, as in the case of lead. (Fig. 4)

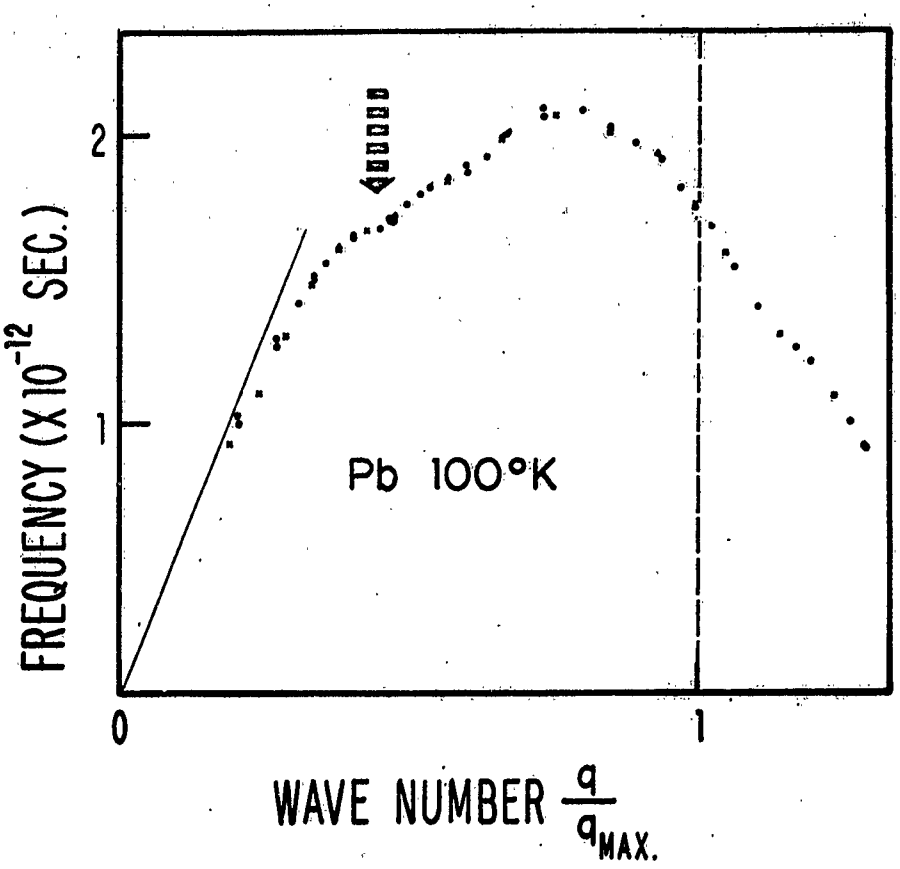

FIGURE 4

Measured longitudinal branch of the phonon dispersion curve for the (110) direction in lead. (After Brockhouse et al; see Ref. 4.) The qualitative similarity of this curve to the theoretical curves of Fig. 3 is striking. The anomaly roughly indicated by the arrow is a "downward" type.

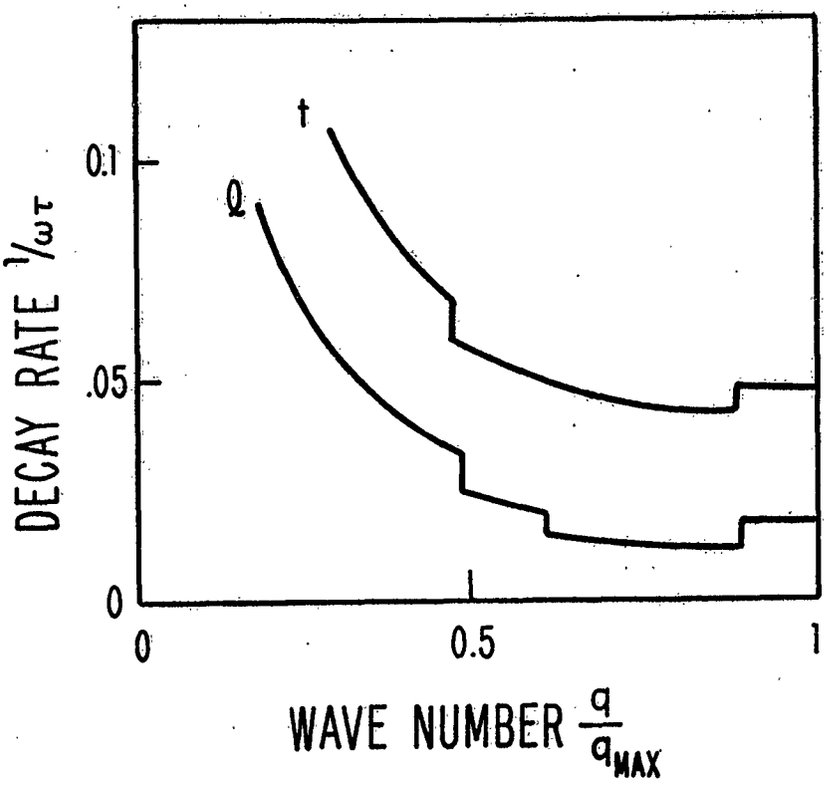

FIGURE 5

Calculated phonon decay rate, expressed as a fraction of frequency, for $\underline{q}$ in the (111) direction. "ℓ" and "t" indicate longitudinal and transverse polarization branches. The Uniform Electron Gas model has been used with constants corresponding to aluminum. Decay rates for small $\underline{q}$ are controlled by more complicated processes, (see Ref. 10) and are not given correctly by these curves. Again, the model used is probably inappropriate for aluminum, but such breaks are expected to appear in other cases.

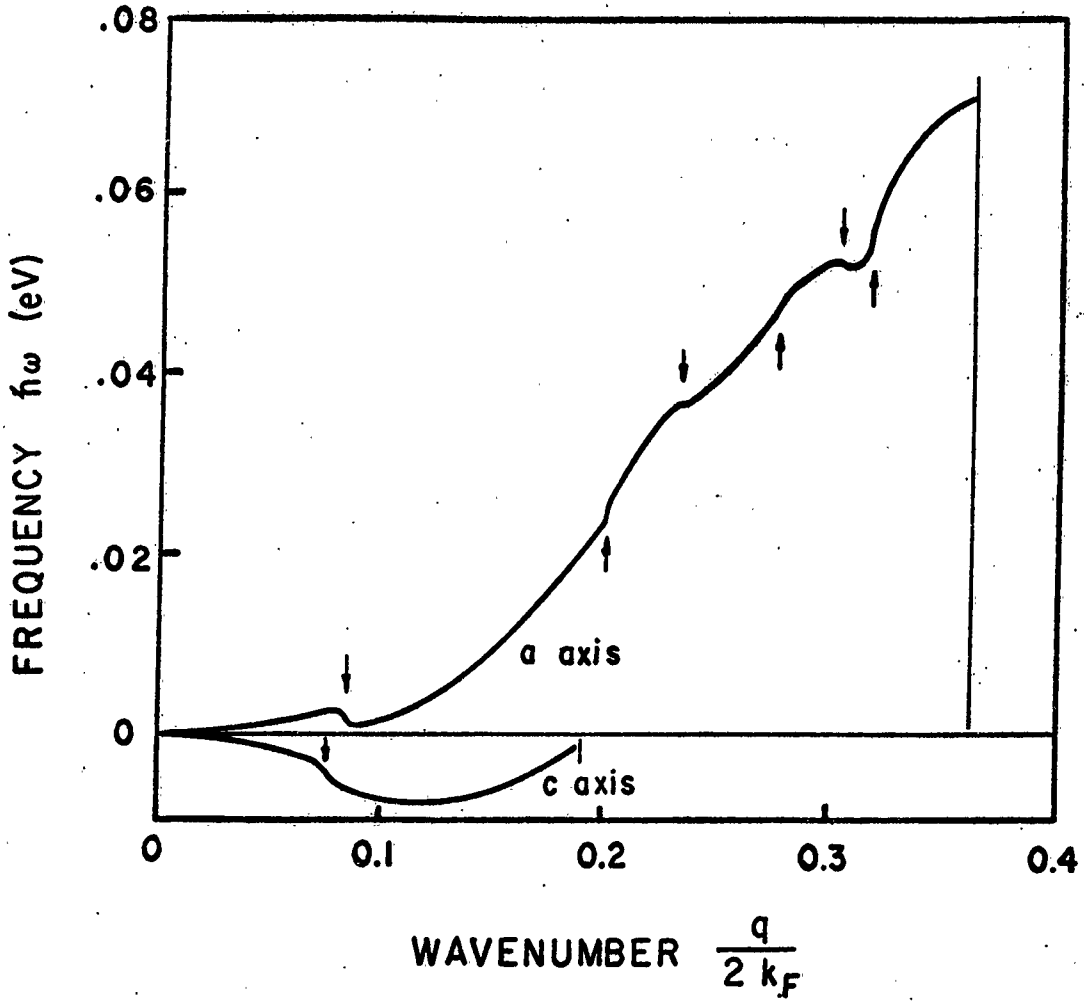

FIGUR E 6

Calculated spin-wave dispersion curves in high-symmetry directions. Fermi surface images are indicated by arrows. Frequency values are calculated using the coupling constant G for gadolinium, derived from the observed resistivity; m^* is taken to be the free-electron mass. Frequencies for other rare-earth metals can be obtained by multiplying by $(g-1)J/7.5$.

FIGURE A1

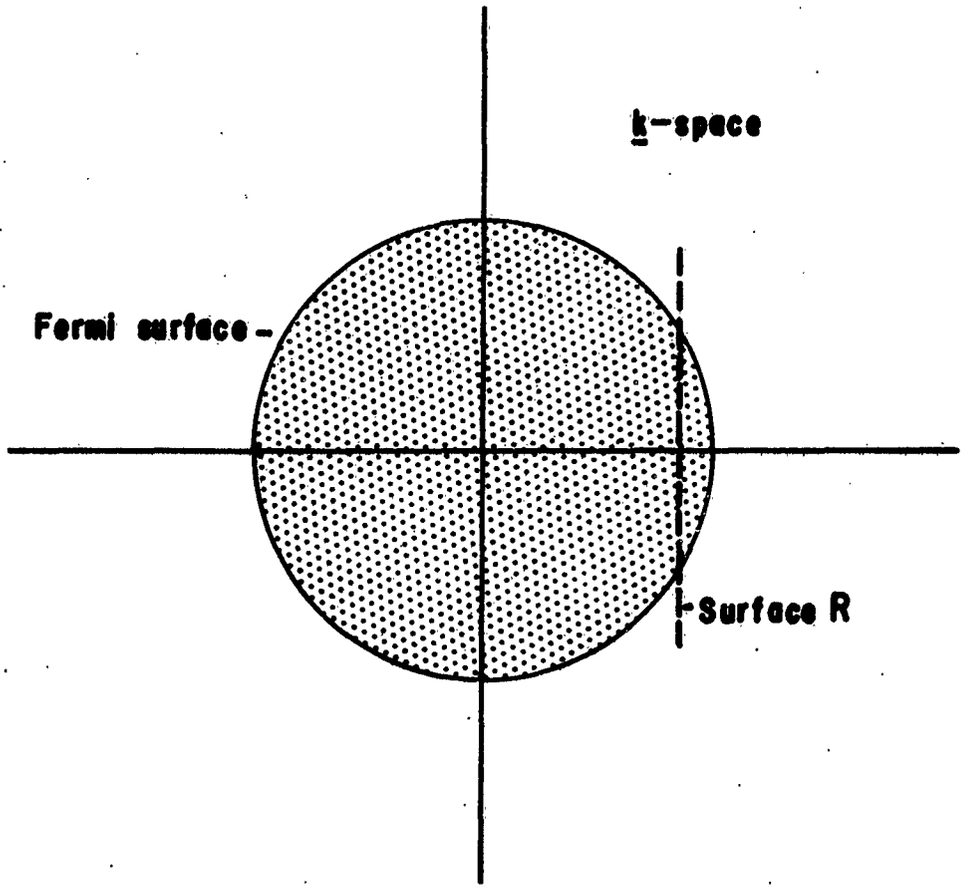

Region of the $\underline{k}$ integration for $W(\underline{p},\omega^+)$. The dashed line represents, for fixed $\underline{p}$ and ω, the surface where the energy denominator of Eq. (A14) vanishes.

FIGURE A2

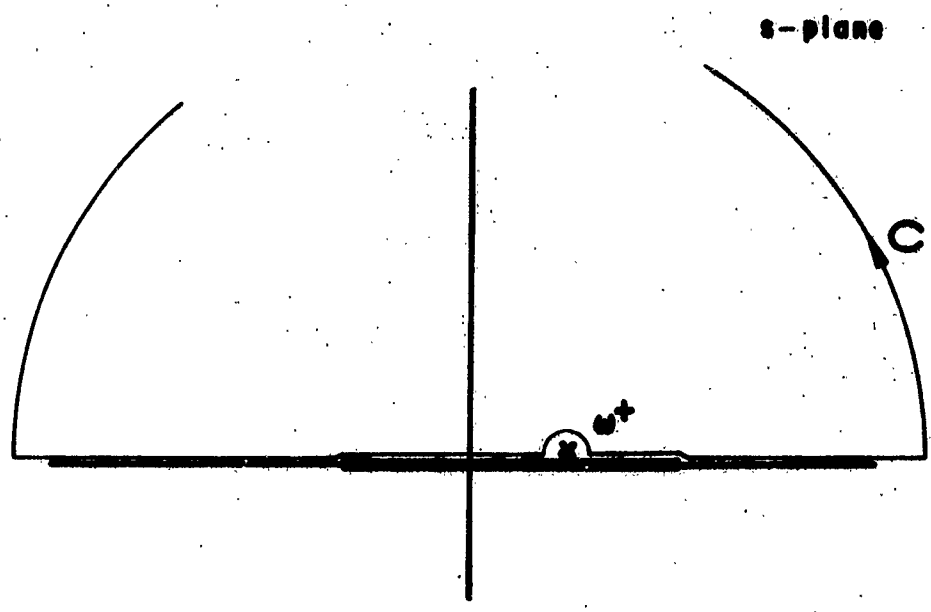

Contour for evaluation of $\mathrm{Re}\{W(\underline{p},\omega^+)\}$

FIGURE A3

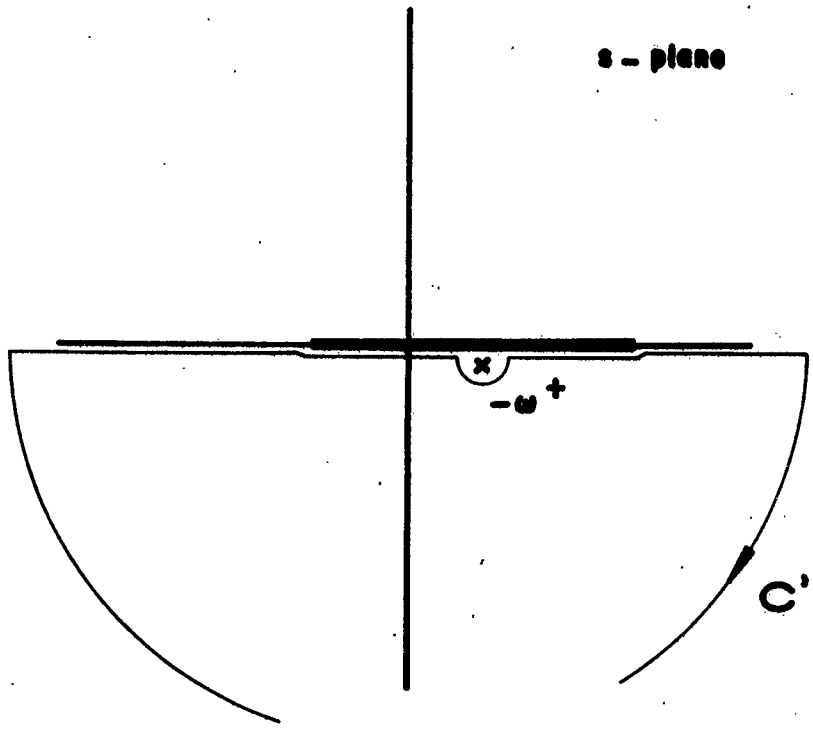

Contour for evaluation of $W(\underline{p},-\omega^+)$.

FIGURE A4

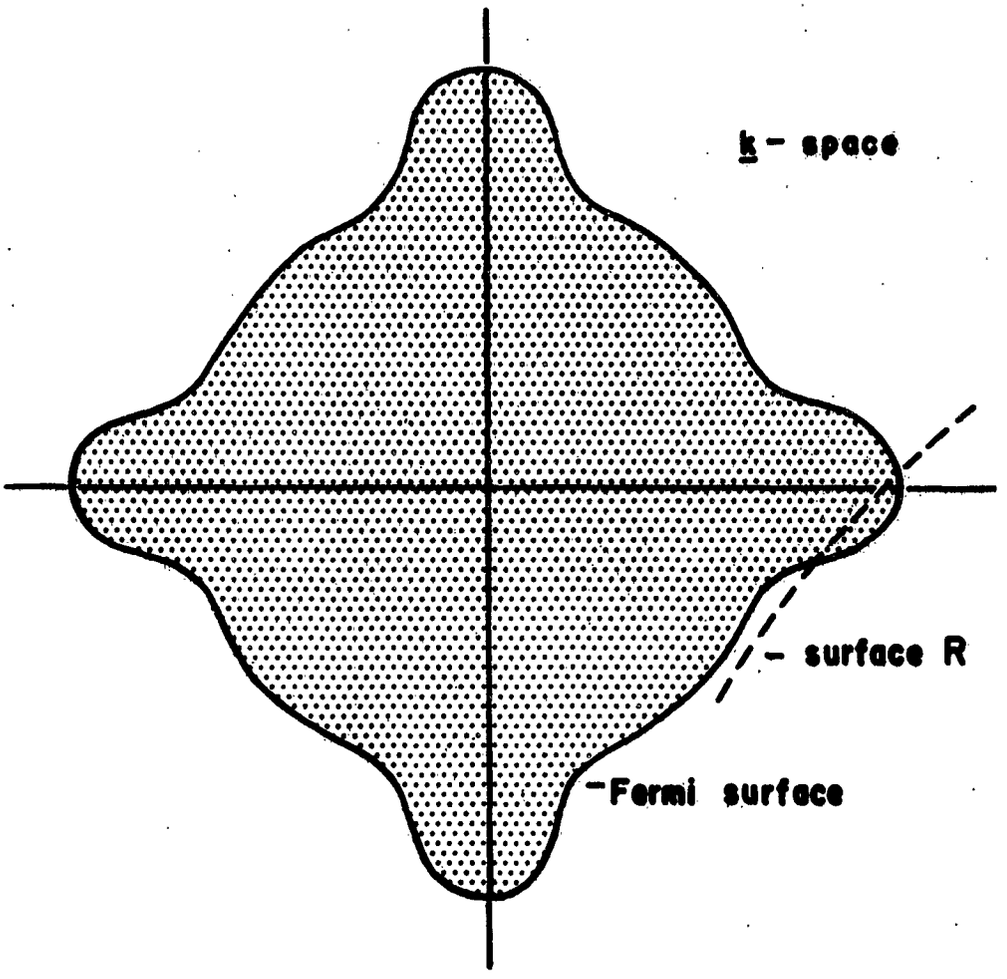

Region of the $\underline{k}$ integration for $W^*(\underline{p},\omega^+)$. The dashed curve represents, for fixed $\underline{p}$ and ω, (near a branch cut) the surface in $\underline{k}$-space on which the energy denominator of Eq. (A27) vanishes.

FIGURE A5

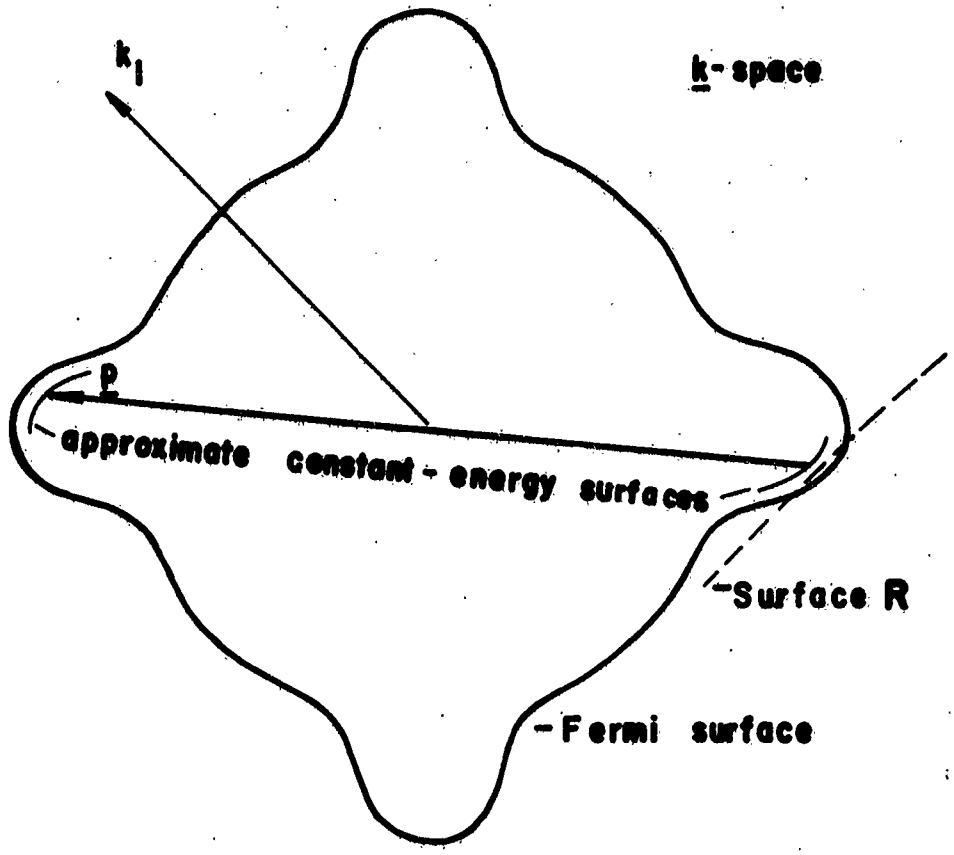

Approximation of the properties of the constant energy surfaces for evaluation of $W^*(\underline{p},\omega^+)$, for ω near the end of the branch cut and $\underline{p}$ approximately a "diameter" of the Fermi surface. The surface R is seen to lie in the region $\underline{k} \simeq -\frac{1}{2}\underline{p}$.

FIGURE A6

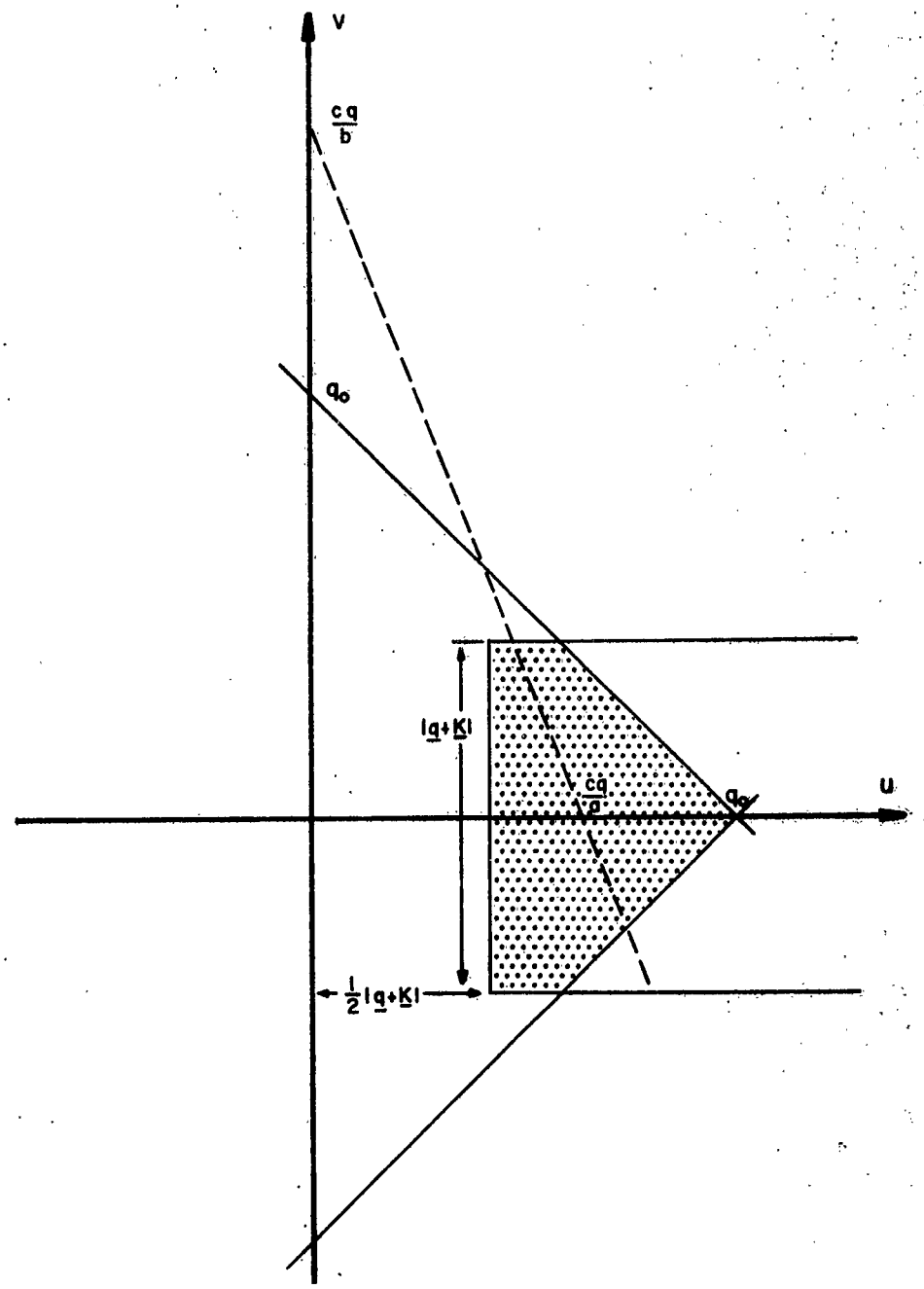

Area of integration in the u,v plane. The δ-function in Eq. (A52) has zero argument along the dashed line.

FIGURE A7

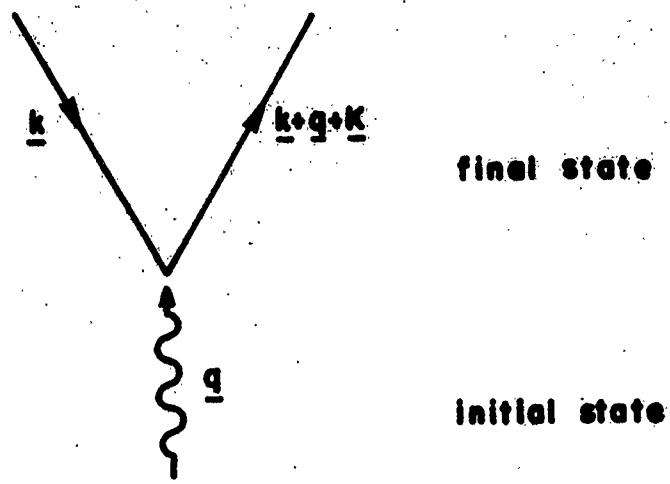

Single-pair creation.

FIGURE A8

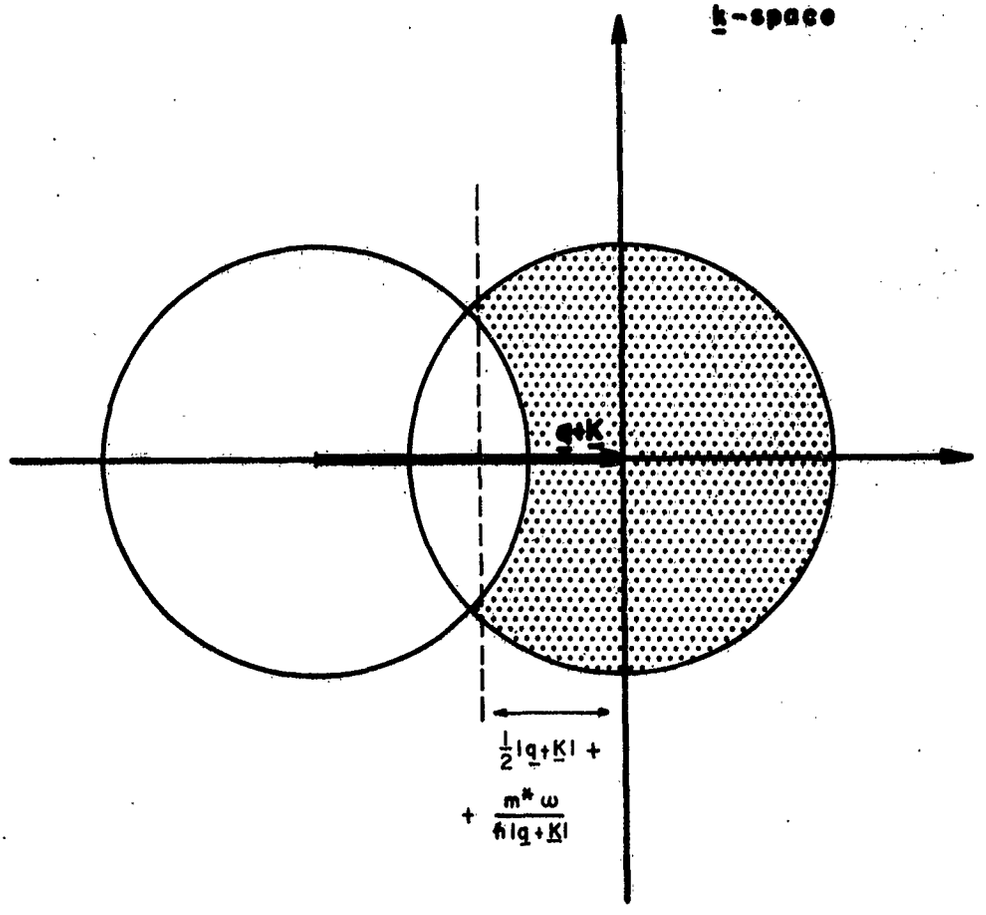

Allowed region for the k integration.

FIGURE A9

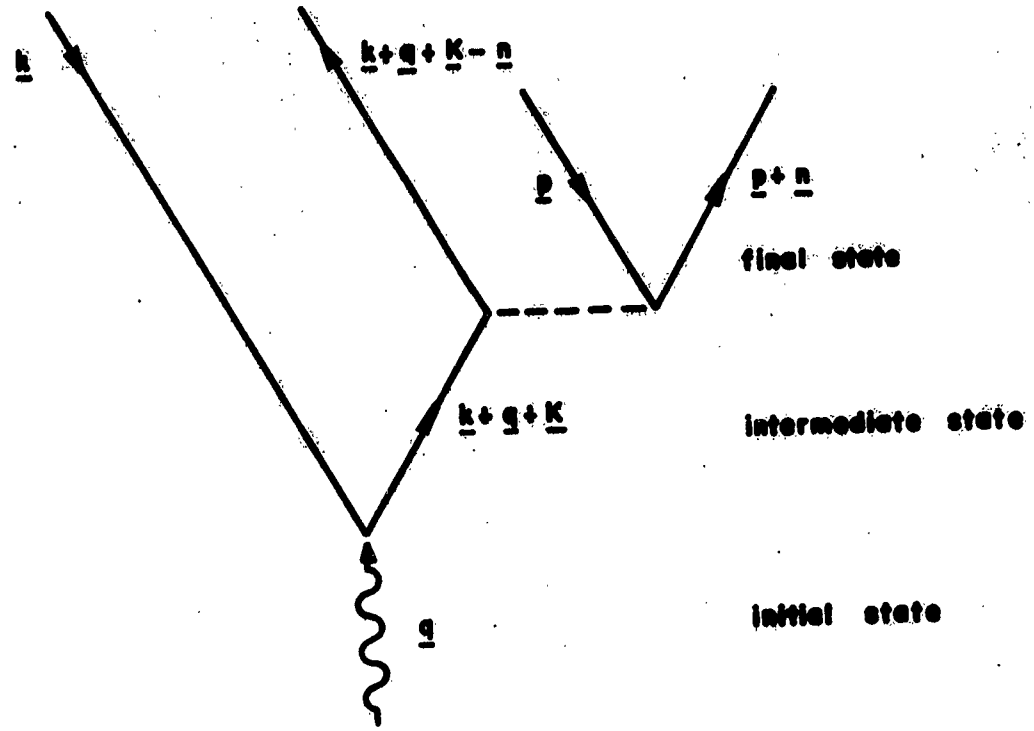

Two-pair creation.

FIGURE A10

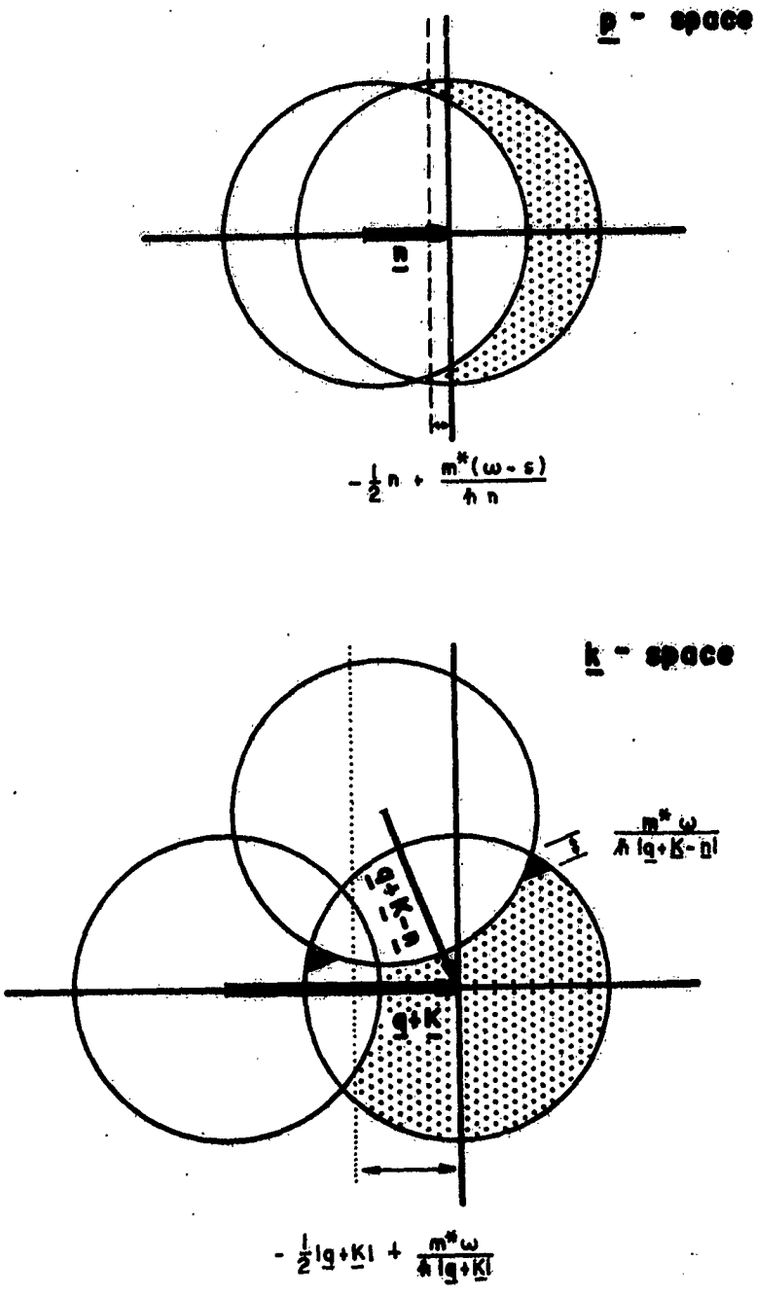

Allowed regions for the $\underline{k}$ and $\underline{p}$ integrations.

OFFICE OF NAVAL RESEARCH
Physics Branch
TECHNICAL REPORTS DISTRIBUTION LIST March, 1962
for

A. Government Distribution

1. Department of Defense

Ass't. Secretary of Defense for Research and Development
Information Office Library Branch
Pentagon Building
Washington 25, D. C. (2 copies)

Armed Services Technical Information Agency
Arlington Hall Station
Attn: TIPCR
Arlington 12, Virginia (10 copies)

2. Department of the Navy

Chief, Bureau of Weapons
Technical Library
Navy Department
Washington 25, D. C.

Chief, Bureau of Ships
Code 300, Technical Library
Navy Department
Washington 25, D. C.

Chief of Naval Research
Office of Naval Research
Attn: Physics Branch (Code 421)
Washington 25, D. C. (3 copies)

Director
Naval Research Laboratory
Technical Information Officer (Code 2000) (6 copies)
Code 2021 (2 copies)
Washington 25, D. C.

Commanding Officer
Office of Naval Research Branch Office
495 Summer Street
Boston 10, Massachusetts (Boston area only)

Commanding Officer
Office of Naval Research Branch Office
346 Broadway
New York 13, New York

Contract Administrator
Southeastern Area
Office of Naval Research
George Washington University
2110 G Street, N. W.
Washington 7, D. C.

Commanding Officer
Office of Naval Research Branch Office
1000 Geary Street
San Francisco 9, California

Commanding Officer
Office of Naval Research Branch Office
86 East Randolph Street
Chicago 1, Illinois

Commanding Officer
Office of Naval Research Branch Office
1030 East Green Street
Pasadena 1, California

Commanding Officer
Office of Naval Research London Branch Office
Navy #100
Fleet Post Office
New York, New York (2 copies)

Librarian
U. S. Naval Post Graduate School
Monterey, California

U. S. Naval Electronics Laboratory
San Diego 52, California

Commanding Officer
U. S. Naval War College
Newport, Rhode Island

Director
Research Department
Naval Ordnance Laboratory
White Oak, Maryland

Commanding Officer
Physics Division
Naval Ordnance Test Station
Inyokern
China Lake, California

Commanding Officer
U. S. Naval Ordnance Laboratory
Corona, California

3. Department of the Air Force

Commanding General
Wright Air Development Center
Wright-Patterson Air Force Base
Dayton, Ohio

Commanding General
Air Research and Development Command
Attn: Office of Scientific Research
Washington 25, D. C. (2 copies)

Commander
Air Force Cambridge Research Center
230 Albany Street
Cambridge, Massachusetts
Attn: CRHCP-1

4. Department of the Army

Commanding Officer
Engineering Research & Development Laboratories
Fort Belvoir, Virginia
Attn: Technical Intelligence Branch

Office of Ordnance Research
Box CM, Duke Station
Durham, North Carolina (2 copies)

Signal Corps Engineering Laboratory
Fort Monmouth, New Jersey
Attn: Technical Information Officer

Dr. J. L. Martin
Watertown Arsenal
Watertown 72, Massachusetts

5. Department of Commerce

Office of Technical Services
Technical Reports Section
Department of Commerce
Washington 25, D. C.

Director
National Bureau of Standards
Washington 25, D. C.

6. Other Agencies

Advanced Research Projects Agency
The Pentagon
Room 3E 157
Washington 25, D. C.

National Aeronautics and Space Administration
1520 H Street Northwest
Washington 25, D. C.

National Research Council
Division of Physical Sciences
National Academy of Sciences
Washington 25, D. C.

Director
National Science Foundation
Washington 25, D. C.

U. S. Atomic Energy Commission
Technical Information Service
P. O. Box 62
Oak Ridge, Tennessee

U. S. Atomic Energy Commission
Washington 25, D. C.

AFSWC, SWRP
Kirtland Air Force Base
New Mexico

Defense Atomic Support Agency
Sandia Base
New Mexico

Dr. Frank Stern
Room 2-004
Naval Ordnance Laboratory
White Oak, Silver Spring, Maryland

Dr. H. P. Frederickse
Solid State Physics Section
National Bureau of Standards
Washington 25, D. C.

Dr. C. W. Beckett
Head and Power Division, Thermodynamics Section
National Bureau of Standards
Washington 25, D. C.

B. Non-Government Distribution

Dr. P. W. Anderson
Bell Telephone Laboratory
Murray Hill, New Jersey

Dr. J. Bardeen
University of Illinois
Urbana, Illinois

Dr. A. Beer
Battelle Memorial Institute
Columbus, Ohio

Professor T. K. Berlin
Department of Physics
The Johns Hopkins University
Baltimore 18, Maryland

Dr. H. Brooks
Division of Applied Sciences
Harvard University
Cambridge, Massachusetts

Professor N. Cabrera
University of Virginia
Charlottesville, Virginia

Professor J. Callaway
Department of Physics
University of California
Riverside, California

Dr. H. B. Callen
University of Pennsylvania
Philadelphia, Pennsylvania

Dr. G. Dresselhaus
Massachusetts Institute of Technology
Lincoln Laboratory
Lexington 73, Massachusetts

Dr. P. P. Ewald
Polytechnic Institute of Brooklyn
99 Livingston Street
Brooklyn 2, New York

Dr. R. A. Ferrell
Department of Physics
University of Maryland
College Park, Maryland

Dr. F. Herman
RCA Laboratories
David Sarnoff Research Center
Princeton, New Jersey

Dr. E. T. Jaynes
Stanford University
Stanford, California

Dr. H. J. Juretschke
Polytechnic Institute of Brooklyn
Brooklyn, New York

Dr. P. E. Kaus
University of Southern California
Los Angeles, California

Dr. A. F. Kip
University of California
Berkeley 4, California

Dr. C. Kittel
Department of Physics
University of California
Berkeley 4, California

Professor J. S. Koehler
University of Illinois
Urbana, Illinois

Professor W. Kohn
Department of Physics
University of California, San Diego
La Jolla, California

Dr. A. V. Lawson
Institute for the Study of Metals
University of Chicago
Chicago 37, Illinois

Professor M. Lax
Syracuse University
Syracuse, New York

Dr. J. M Luttinger
Department of Physics
Columbia University
New York 27, New York

Dr. H. E. Meijer
Catholic University
Washington, D. C.

Dr. Gordon Newell
Division of Applied Mathematics
Brown University
Providence, Rhode Island

Dr. A. W. Overhauser
Ford Research Laboratory
Dearborn, Michigan

Dr. A. M. Parks
Department of Physics
University of California
Berkeley 4, California

Dr. W. Paul
Harvard University
Cambridge, Massachusetts

Dr. Linus Pauling
California Institute of Technology
Pasadena, California

Dr. Frederick Seitz
Department of Physics
University of Illinois
Urbana, Illinois

Dr. C. H. Shaw
Department of Physics
Ohio State University
Columbus 10, Ohio

Dr. W. Shockley
Shockley Transistor Corporation
Mountain View, California

Dr. John C. Slater
Department of Physics
Massachusetts Institute of Technology
Cambridge, Massachusetts

Dr. C. S. Smith
Institute for the Study of Metals
University of Chicago
Chicago 37, Illinois

Dr. L. P. Smith
Department of Physics
Cornell University
Ithaca, New York

Professor J. S. Toll
University of Maryland
College Park, Maryland

Professor A. R. von Hippel
Massachusetts Institute of Technology
Laboratory for Insulating Research
Cambridge 39, Massachusetts

Dr. G. Wannier
Bell Telephone Laboratory
Murray Hill, New Jersey

Dr. W. K. R. Watson
University of Southern California
Los Angeles, California

Dr. P. R. Weiss
Rutgers University
New Brunswick, New Jersey